

1 **Characteristics of consecutive tsunamis and resulting**

2 **tsunami behaviors in southern Taiwan induced by the**

3 **Hengchun earthquake doublet on 26 December 2006**

4 An-Chi Cheng^{1,2}, Anawat Suppasri^{2,3}, Kwanchai Pakoksung³, Fumihiko Imamura^{2,3}

5 ¹Civil and Environmental Engineering, Graduate School of Engineering, Tohoku University, 6-6-06 Aoba,
6 Aramaki-Aza, Aoba, Sendai 980-0845, Japan

7 ²WISE Program for sustainability in the Dynamic Earth, Tohoku University, 6-3 Aoba, Aramaki Aza, Aoba,
8 Sendai 980-8578, Japan

9 ³International Research Institute of Disaster Science, Tohoku University, 468-1 Aoba, Aramaki-Aza, Aoba,
10 Sendai 980-0845, Japan

11 *Correspondence to:* An-Chi Cheng (cheng.anchi.r6@dc.tohoku.ac.jp)

12
13 **Abstract.** Consecutive $M_L7.0$ submarine earthquakes occurred offshore the Hengchun Peninsula, Taiwan,
14 on 26 December 2006. A small tsunami was generated and recorded at tide gauge stations. This important
15 event attracted public interest, as it was generated by an earthquake doublet and produced a tsunami risk
16 for Taiwan. This study analyzed tide gauge tsunami waveforms and conducted numerical simulations to
17 understand the source characteristics and resulting behaviors of tsunamis. The maximum wave heights at
18 the three stations were 0.08 m (Kaohsiung), 0.12 m (Dongkung), and 0.3 m (Houbihu), and only Houbihu
19 recorded the first wave crest as the largest. The tsunami duration was 3.9 h at Dongkung and over 6 h at
20 Kaohsiung and Houbihu. Spectral analyses detected dominant periodic components of spectral peaks on
21 the tsunami waveforms. The period band from 13.6-23.1 min was identified as the tsunami source spectrum,
22 and the approximate fault area for the consecutive tsunamis was estimated to be 800 km², with central fault
23 depths of 20 km (first earthquake) and 33 km (second earthquake). The focal mechanisms of the first
24 earthquake, with a strike of 319°, dip of 69°, and rake of -102°, and the second earthquake, with a strike of
25 151°, dip of 48°, and rake of 0°, could successfully reproduce the observed tsunami waveforms. Numerical
26 simulations suggested that the tsunami waves were coastally trapped on the south coast of Taiwan during
27 the tsunami's passage. The trapped waves propagated along the coast as edge waves, which repeatedly
28 reflected and refracted among the shelves, interfered with incoming incident waves, and resonated with the
29 fundamental modes of the shelves, amplifying and continuing the tsunami wave oscillation. These results
30 elucidated the generation and consequential behaviors of the 2006 tsunami in southern Taiwan, contributing
31 essential information for tsunami warning and coastal emergency response in Taiwan to reduce disaster risk.

32 33 **1. Introduction**

34 Taiwan is located at the southeast margin of the Eurasian plate and the Philippine Sea plate. The abrupt
35 movement of plates results in active seismic activity at the boundary area, such as in the Manila Trench and
36 Ryukyu Trench. The Manila Trench and Ryukyu Trench are located in offshore Taiwan and have been
37 identified as hazardous tsunamigenic regions, as both have the potential to generate megathrust earthquakes
38 and cause severe tsunami impacts on coastal plains (Liu et al., 2009; Megawati et al., 2009; Wu and Huang,
39 2009; Li et al., 2016; Sun et al., 2018; Qiu et al., 2019). In addition to potential megathrust earthquakes,
40 historical earthquake tsunamis in Taiwan are well recorded in ancient and written documents. Examples
41 include the 1781/1782 Jiateng Harbor flooding and tsunami event (Okal et al., 2011; Li et al., 2015) and
42 the 1867 northern Taiwan earthquake (Cheng et al., 2016; Sugawara et al., 2019).

43 Two large earthquakes occurred off the coast of Hengchun Peninsula, Taiwan, on 26 December 2006.
44 The first earthquake occurred at 12:26:21 UTC (i.e., 20:26:21 Taiwan Standard Time) and was followed by
45 a second earthquake 8 min later at 12:34:15 UTC (i.e., 20:34:15 Taiwan Standard Time). The Central
46 Weather Bureau (CWB) catalog (R.O.C.) located the epicenter of the first shock at 21.69° N and 120.56° E
47 and that of the second shock at 21.97° N and 120.42° E. The locations of the Hengchun Peninsula and the
48 epicenters of the successive earthquakes are shown in Figure 1.

49 The respective magnitudes of these two earthquakes were suggested to be $M_L = 7.0$ ($M_w = 7.0$ in the
50 Global Centroid Moment Tensor (CMT) catalog) for the former and $M_L = 7.0$ ($M_w = 6.9$ in the Global CMT
51 catalog) for the latter. From a seismological perspective, pairs of large earthquakes with equivalent fault
52 sizes that occur in similar spatial and temporal proximities are referred to as doublets (Lay and Kanamori,
53 1980; Kagan and Jackson, 1999). As they shared comparable earthquake magnitudes and very close
54 epicenters and occurrence times, the successive earthquakes on 26 December 2006 are considered an
55 earthquake doublet event (Ma and Liang, 2008; Wu et al., 2009). These 2006 earthquakes in southern
56 Taiwan were considered the largest event in the past hundred years. Several casualties and some structural
57 damages were reported in southern Taiwan during this seismic event (National Disaster prevention and
58 Protection Commission, R.O.C., 2007). The tectonic settings of the 2006 earthquake doublet are shown in
59 Figure 2.

60 A small tsunami was generated after the successive strong motions of these earthquakes. The tsunami
61 propagated toward and reached the western coast of southern Taiwan immediately after the earthquakes.
62 Although no coastal run-up or inundation was reported, tsunami signals were instrumentally recorded at
63 CWB tide gauge stations in southern Taiwan. The December 2006 tsunami was an important event that
64 attracted public interest, as it was unique not only because it was generated by earthquakes in short
65 succession but also because it was a new occurrence for ordinary citizens in Taiwan. This recent tsunami
66 not only corroborates the tsunami risk in Taiwan but also increases awareness of disaster risk management,
67 such as preparedness and mitigation countermeasures for future tsunamis.

68 The tsunami observations that were reported following the 26 December 2006 tsunami also raised some
69 questions. First, the first tsunami wave crest was not shown to be the largest at some stations. This amplified

70 tsunami wave is considered an important issue for tsunami warnings, as a higher later wave could suddenly
71 upgrade the threat level of the tsunami (Suppasri et al., 2017; Suppasri et al., 2021). Second, the tsunami
72 oscillation recorded at some stations lasted for more than 6 h following the earthquakes. This indicated that
73 the high-energy waves persisted along the coast without decay during the 2006 tsunami and were considered
74 one of the cascading risks of tsunamis, as they could further intensify the damaging impacts of the tsunamis
75 on the coastal region.

76 The other issue was to identify which source models could better explain the successive tsunamis
77 compared to the recorded observations in southern Taiwan. Wu et al. (2008) simulated the tsunami from
78 this event using single fault models. They numerically computed the tsunami propagation on a nested grid
79 system with fine-grid of 0.125 arc min resolution bathymetry data and compared their results with
80 observational data from tide gauge stations. Although the source models for this tsunami event have been
81 specified and modeled in previous studies, the uncertainty and variability aspects of these models and the
82 bathymetry have not been thoroughly investigated. These uncertainties in earthquake fault parameters and
83 significant differences among open-source bathymetries can exaggerate the modeled results compared to
84 the predictions of previous studies to the 2006 tsunami. Therefore, it is critical to discuss these model
85 performances from a sensibility perspective because it is desirable to obtain a tsunami source model and to
86 understand the reliability of bathymetry data that is utilized for numerical simulation to reasonably estimate
87 the tsunami wave activities of the 2006 tsunami.

88 Based on the above background, the primary intent of this article is to address all aforementioned issues
89 related to the 2006 tsunami that have not been previously discussed and to provide some results. The content
90 of this article is organized as follows. First, the observed tsunami waveforms are analyzed to determine the
91 physical characteristics of the tsunami and employed as inputs for root mean square (RMS) analyses to
92 detect the tsunami duration. Second, spectral analyses are performed to detect the periodic components of
93 the tsunami waves based on the identification of the tsunami source spectrum and resonance modes. Then,
94 a sensitivity analysis of the source models and open-source bathymetries is conducted based on the
95 simulated waveforms from forward tsunami simulations. The mechanism of tsunami wave trapping around
96 southern Taiwan is examined based on the comparison of modeled results from numerical experiments
97 using actual and manipulated bathymetry. The December 2006 earthquake tsunami represents a unique and
98 recent incident in Taiwan; therefore, these findings could not only help further clarify tsunami generation
99 and the important behaviors responsible for tsunami hazards facing the island of Taiwan but also have
100 implications for tsunami warning and disaster risk management.

102 **2. Data and methods**

103 **2.1 Tide gauge tsunami data**

104 Time history data of sea levels that are recorded at coastal sites provide one source of information that
105 we can use to study tsunami patterns. To investigate the characteristics of the 2006 tsunami, sea level

106 records from tide gauge stations were employed for analysis in the present study. For this purpose, the
 107 recorded data from three tide gauge stations (Kaohsiung, Dongkung, and Houbihu) located in southern
 108 Taiwan were obtained. These tide gauge stations are operated and maintained by the CWB, R.O.C. All
 109 stations recorded sea levels at a sampling rate of 6 min. In this doublet event, the first and second
 110 earthquakes occurred at 20:26:21 and 20:34:15 (Taiwan Standard Time), respectively. Hence, 28 h of tide
 111 gauge records (from 8:00 on 26 December 2006 to 12:00 on 27 December 2006, Taiwan Standard Time)
 112 were adopted for analysis. To approximate the wave components of the tsunami and to remove the low-
 113 frequency noise that was attributed to the tidal effect, the sea level records at the tide gauge stations were
 114 de-tided by removing the long-period (> 2 h) tidal constituents. The original data recorded at the tide gauge
 115 stations in southern Taiwan are shown in Figure 2a, and the de-tided data are presented in Figure 2b. The
 116 locations of the tide gauge stations are shown in Figure 3.

117 The tsunami durations represent the observation time of high-energy tsunami waves persisting at a
 118 coastal site. The tsunami durations at all the stations were identified based on a calculation of root mean
 119 square (RMS) sea levels, indicating the elapsed time of the wave amplitude above the normal oscillation
 120 level before the tsunami wave arrived (Heidarzadeh, 2021). The RMS analysis calculated the moving
 121 average of the recorded sea level along a moving time window of 24 min. The calculation for RMS sea
 122 level is presented in equation (1):

$$S(t) = \sqrt{\frac{1}{w} \int_{t-\frac{w}{2}}^{t+\frac{w}{2}} h(x)^2 dx} \quad (1)$$

123
 124 In this equation, $S(t)$ represents the RMS sea level at time step t , $h(t)$ denotes the recorded sea level at time
 125 t , and w stands for the moving time window. In the present study, the length of the tsunami data employed
 126 for RMS analysis is 12 h, which includes 120 data points, ranging from 17:00 on 26 December 2006 to
 127 5:00 on 27 December 2006 (Taiwan Standard Time). A similar method has been applied in the research by
 128 Hayashi et al. (2012).

129

130 **2.2 Spectral analyses**

131 To apply spectral analyses to the tsunami data, two types of analyses were included and processed in this
 132 study: the Fourier analysis and the wavelet (time-frequency) analysis. The Fourier analysis is based on the
 133 fast Fourier transform (FFT) algorithm and applied based on the updated open-source library, Numpy, in
 134 the Python package (Harris et al., 2020). The Fourier analysis was performed to estimate the spectral
 135 components of the time history data of the tsunami waveform. The entire dataset of the tsunami waveform
 136 inputted for Fourier analysis covered 600 min, which included 100 data points ranging from 5 h before to
 137 5 h after the tsunami, as the sampling rate of the data was 6 min. The Fourier analysis was separately applied
 138 to the de-tided background (i.e., 5 h data before the tsunami arrival) and the tsunami signals (i.e., 5 h data

139 after tsunami arrival) to identify significant changes in the spectral energy associated with the tsunami.
 140 Additionally, the spectral ratio was computed for the tsunami spectra to exclude the local modes of coastal
 141 sites from the periodic components. Wavelet analysis was computed based on the Morlet mother function,
 142 as suggested by Torrence and Compo (1988). Wavelet analysis detects the periodic change in spectral peaks
 143 over time. The length of the tsunami data input in the wavelet analysis was 15 h (15:00 on 26 December
 144 2006 to 06:00 on 27 December 2006, Taiwan Standard Time). A similar method has been widely applied to
 145 solve time-frequency problems for many recent tsunami events, such as the 2018 Sulawesi tsunami in
 146 Indonesia and the 2020 Aegean Sea earthquake tsunami (Heidarzadeh, 2019; Heidarzadeh, 2021).

147

148 **2.3 Numerical tsunami simulation**

149 Numerical simulation is a computer-based method that describes equations for the motion of tsunami
 150 wave propagation. Tsunami wave propagation can be numerically modeled based on various theories,
 151 including shallow water and dispersive wave theories. Among those theories, the shallow water equations
 152 are some of the most commonly used methods to model tsunami propagation from the source to nearshore
 153 areas. Various computational models have been developed to solve shallow water equations, and the
 154 TUNAMI (Tohoku University Numerical Analysis Model for Investigation of tsunamis) code is one of the
 155 widely used models to numerically simulate both far-field and near-field tsunamis (Suppasri et al., 2010;
 156 Suppasri et al., 2014). The second version of the TUNAMI code (TUNAMI-N2) was mainly developed to
 157 deal with near-field tsunamis by applying the nonlinear theory of shallow water equations, which is solved
 158 using a leap-frog scheme (Imamura, 1995). Since the 2006 tsunami presented as a near-field tsunami in
 159 Taiwan, the TUNAMI-N2 model was used in this study to simulate the 2006 tsunami with nonlinear shallow
 160 water equations. The nonlinear shallow water equations on the Cartesian coordinate system are presented
 161 in equations (2)-(4), and the nonlinear equations are solved by applying the finite difference method:

$$\frac{\partial \eta}{\partial t} + \frac{\partial M}{\partial x} + \frac{\partial N}{\partial y} = 0 \quad (2)$$

$$\frac{\partial M}{\partial t} + \frac{\partial}{\partial x} \left(\frac{M^2}{D} \right) + \frac{\partial}{\partial y} \left(\frac{MN}{D} \right) + gD \frac{\partial \eta}{\partial x} + \frac{gn^2}{D^3} M \sqrt{M^2 + N^2} = 0 \quad (3)$$

$$\frac{\partial N}{\partial t} + \frac{\partial}{\partial x} \left(\frac{MN}{D} \right) + \frac{\partial}{\partial y} \left(\frac{N^2}{D} \right) + gD \frac{\partial \eta}{\partial y} + \frac{gn^2}{D^3} N \sqrt{M^2 + N^2} = 0 \quad (4)$$

162 In these equations, η is the water level, M and N are the discharge fluxes in the x and y directions,
 163 respectively, D is the total water depth, g is the gravitational acceleration, and n is Manning's roughness
 164 coefficient. The bottom friction term was represented by the Manning roughness coefficient, which was set
 165 as $0.025 \text{ s m}^{-1/3}$, assuming that the seafloor in the model domain is in perfect condition. The numerical
 166 tsunami simulations were conducted with a time interval of 0.1 s and grid intervals of 450 m. The entire
 167 model domain covered the source region and southern Taiwan, which comprised mesh numbers of 538 and
 168 631 in the x and y directions, respectively. The time interval and grid intervals were set up to satisfy the

169 Courant–Friedrichs–Lewy (CFL) condition to ensure the stability of the simulation. The CFL condition is
170 presented in equation (5):

$$\Delta t \leq \frac{\Delta x}{\sqrt{2gh_{max}}} \quad (5)$$

171 where Δt is the time interval, Δx is the grid spacing, and h_{max} is the maximum water depth in the model
172 domain. As the initial condition inputted for numerical tsunami simulation, the initial water level
173 distribution was calculated from the earthquake fault parameters using the theory of Okada (1985). In
174 addition, the horizontal deformation contribution to tsunami generation on steep bathymetric slopes
175 (Tanioka and Satake, 1996) was included. The calculation conditions for the numerical tsunami simulation
176 are summarized in Table 1.

177

178 **2.4 Sensitivity analyses of source models**

179 **2.4.1 Single fault models**

180 Multiple forward tsunami simulations were conducted using single fault models with different fault
181 depths and fault orientations. The main goal of the multiple forward tsunami simulations was to find a
182 single fault model that could produce tsunami waveforms that were highly consistent with the tide gauge
183 station observations in southern Taiwan.

184 There were two moment tensor solutions available from the Global Centroid Moment Tensor (GCMT)
185 Project and United States Geological Survey (USGS) for the successive earthquakes on 26 December 2006
186 (Figure 2.). Each solution suggested two possible fault planes for those earthquakes. The focal mechanisms
187 for the two earthquakes estimated by the GCMT and USGS are summarized in Table 2. Through the analysis
188 of the tsunami waveforms simulated by the multiple forward tsunami simulations, one of those fault planes
189 could be chosen as the appropriate fault plane for the respective earthquakes of the 2006 earthquake doublet.
190 A similar approach has been applied in a previous study to obtain the optimum fault plane for the 2016
191 Fukushima normal faulting earthquake (Gusman et al., 2017).

192 Wu et al. (2008) computed synthetic tsunami waveforms based on single fault models using different
193 fault planes of the GCMT solutions. They found that the nodal plane (NP) of NP2 of the first earthquake,
194 with a strike of 329°, dip of 61°, and rake of -98°, and the fault plane of NP1 for the second earthquake,
195 with a strike of 151°, dip of 48°, and rake of 0°, produced tsunami waveforms that better fit the observed
196 data.

197 Based on the study conducted by Wu et al. (2008), the focal mechanisms of NP2 to the first earthquake
198 and NP1 to the second earthquake from the GCMT solution were used for a sensitivity analysis of fault
199 depths. An approximated fault area with a 40 km length and a 20 km width (fault size = 800 km²) was
200 estimated for the successive earthquakes based on the empirical formula with tsunami source periods. The
201 methods by which the fault area of the two earthquakes was obtained are discussed in section 4.1. For the
202 given moment magnitude (M_w) values of the 7.0 and 6.9 earthquakes, the amount of average slip can be

203 estimated to be 1.66 m for the first earthquake (i.e., M_w 7.0) and 1.17 m for the second earthquake (M_w 6.9),
 204 assuming a rigidity of 30 Gpa. The centroid depths of the GCMT (20 km) and USGS (25 km) solutions for
 205 the first earthquake are significantly different, while a similar depth of 33 km was estimated from both
 206 solutions for the second earthquake. Therefore, for the sensitivity analysis of central fault depth, the central
 207 fault depths of 15, 20, 25, and 35 km of the first earthquake were evaluated.

208 After determining the best central fault depth for the single fault models of the two earthquakes, multiple
 209 tsunami forward simulations were applied to all possible fault planes from the moment tensor solutions
 210 estimated by GCMT and USGS using a single fault. The misfit of observed and simulated tsunami
 211 waveforms from the multiple tsunami forward simulations was calculated and compared to examine the
 212 focal mechanisms that better explain the observed tsunami data. The misfit of the observed and simulated
 213 tsunami waveforms can be calculated using equation (6):

$$\varepsilon = \frac{1}{N} \sqrt{\sum_{i=1}^N \frac{(Obs_i - Sim_i)^2}{(Obs_i)^2}} \quad (6)$$

214 where ε is the misfit of the observed and synthetic tsunami waveforms, N is the total number of data
 215 points, Obs_i is the observed data at time step i , and Sim_i is the simulated data at time step i . Equation
 216 (8) calculates ε for one station. For cases with several stations, the overall misfit is obtained from the mean
 217 of the ε values computed from all the stations.

218

219 **2.4.2 Multiple fault models**

220 After determining the best central fault depths and fault orientations of a single fault, the area of each
 221 single fault was subdivided into 8 subfaults with areas of 10 km \times 10 km, with 4 and 2 subfaults along
 222 the strike and dip axes, respectively. The locations of each subfault in the fault model of the two earthquakes
 223 are shown in Figure 4. The top depths for the two earthquakes are 15.3 km and 29.1 km, which correspond
 224 to subfaults 1-4 in each fault model (Figure 4a, b). The rest of the depths from the shallowest to the deepest
 225 portion along the dip axis are derived using fault parameters of width dimensions and dip angles. The
 226 respective fault parameters of each subfault in the fault models of the two earthquakes are summarized in
 227 Table 3.

228 The tsunami sensitivity to the non-uniform slip distribution of the fault model was evaluated. For that
 229 purpose, two slip levels for each subfault were established, namely, the large (asperity) slip and the
 230 background slip region of the entire fault. The large slip and background slip region should satisfy the M_w
 231 to avoid overestimation. The slip amount in each region was obtained using the following procedures. First,
 232 the amount of average slip (D_a) was calculated using the M_w , the entire fault area (S), and a rigidity (μ) of
 233 30 GPa, per the equations introduced by Kanamori (1977):

$$M_w = \frac{\log M_0 - 9.1}{1.5} \quad (7)$$

$$D_a = \frac{M_0}{\mu S} \quad (8)$$

234 Next, the amount of large slip ($2D_a$) was assumed to be twice that of the average slip based on a 2017
 235 tsunami receipt report. The total area of the large slip area (S') was set to be 25% of the entire fault area,
 236 and the seismic moment of the large slip area (M_0') can be obtained using equation (8). Then, the slip
 237 amount of the background area (D_b) can be estimated using the area of the background region (S_b) following
 238 equations (8)-(9):

$$S_b = S - S' \quad (8)$$

$$D_b = \frac{M_0 - M_0'}{\mu S_b} \quad (9)$$

239 The details of the slip amount in each region for the two earthquakes are summarized in Table 4a.

240 After determining the slip amount of the asperity and background regions, the tsunami sensitivity to the
 241 non-uniform fault slip distribution was studied. The asperity area with the large slip was located in the
 242 shallow portion of the entire fault area based on information from the 2011 Tohoku-Oki earthquake (Satake
 243 et al., 2013; Fukutani et al., 2021), focusing on the north (subfaults 3-4), central (subfaults 2-3), and south
 244 (subfaults 1-2) parts of each earthquake fault model. Assuming different asperity locations for the two
 245 earthquakes, a total of 9 scenarios were simulated. The multiple fault models and the generated tsunamis
 246 of each earthquake are shown in Figures 5 And 6. The asperity locations of multiple fault models for the
 247 two earthquakes in each scenario are summarized in Table 4b.

248

249 **2.5 Tsunami simulation using open-source bathymetry data**

250 In addition to the fault parameters of the source models, bathymetry data are needed for simulating
 251 tsunami wave propagation. Simulated tsunami propagation results are known to be sensitive to the accuracy
 252 and resolution of bathymetry data. Although it can be expected that bathymetry data with a higher accuracy
 253 and resolution can produce simulated results that better fit the actual values, such data are not always
 254 available and freely accessible. Due to this limitation, open-source datasets have often been utilized for
 255 modeling tsunamis in many previous studies (Koshimura et al., 2008; Suppasri et al., 2012; Li et al., 2016;
 256 Otake et al., 2020).

257 Unfortunately, open-source datasets are sometimes problematic and insufficient for the accurate
 258 simulation of tsunami waves because they lack accurate, quality data (Griffin et al., 2015). A similar issue
 259 has been reported by Zengaffinen et al. (2021) and Heidarzadeh et al. (2019) in simulating the 2018 Anak
 260 Krakatoa tsunami and the 2018 Sulawesi tsunami. Significant differences in various sources of datasets can
 261 also result in modeled results that in contrast to values from previous studies. Therefore, , it is important to
 262 assess and note different available open-source bathymetries in relation to model performances for purpose
 263 of tsunami hazard assessment..

264 For this purpose, a tsunami simulation was separately applied to two different sources of bathymetry data,
265 namely, General Bathymetric Chart of the Oceans (GEBCO) data and ETOPO1 data, and the misfit between
266 the modeled results was evaluated. The GEBCO data contain bathymetry data with grid intervals of 15 arc
267 seconds, while ETOPO1 data have sea depth data with a resolution of 1 arc minute. To fairly investigate
268 the model performances from different datasets, bathymetry data from the two datasets were converted to
269 450 m grids and used as the input for the numerical tsunami simulations. Figure 7 Shows the bathymetry
270 data of the modeled domain obtained from GEBCO and ETOPO1 data. As the initial condition, the
271 simulated initial water distribution of the tsunami generated by the proposed multiple fault model (LS2)
272 was used for these simulations, in which the asperity locations of the two earthquakes were assumed to be
273 at the center of the entire fault area.

274

275 **2.6 Evaluation of the bathymetry effect on tsunami wave trapping**

276 To examine any significant change in tsunami wave transmission that could be attributed to the
277 bathymetry effect during the passage of the 2006 tsunami, numerical experiments (MS, EXP1, EXP2) for
278 tsunami propagation were conducted using actual and manipulated bathymetry data. For the main
279 simulation (MS) numerical experiment, actual GEBCO bathymetry data with a resolution of 450 m derived
280 from sea depth data with grid intervals of 15 arc seconds were used. For the manipulated bathymetry data
281 that were used for numerical experiment EXP1, sea depths greater than 500 m were replaced with 500 m
282 depths. For numerical experiment EXP2, the bathymetry data were manipulated by removing sea depth
283 data with a flattened sea bottom at a depth of 500 m. The 500 m depth was specified because the bathymetric
284 slopes are very gentle at sea depths shallower than 500 m near southern Taiwan, and the area is therefore
285 considered a shelf region. Figure 8 Shows the map-manipulated bathymetry of the model domain for
286 numerical experiments EXP1 and EXP2. The details of the bathymetry data used for numerical experiments
287 MS, EXP1, and EXP2 are summarized in Table 5.

288 The results of the numerical experiments were compared to examine how tsunami wave directivity could
289 change due to the bathymetric effect and to evaluate how much tsunami wave energy could be coastally
290 trapped in different bathymetric conditions during the passage of the tsunami.

291

292 **3. Analyses of tsunami waveforms and durations**

293 **3.1 Physical characteristics of tsunami waveforms**

294 The December 2006 earthquake tsunami was observed at several tide gauges located along the
295 southwestern coast of Taiwan. The tsunami observations are plotted in Figure 9a. The initial wave arrived
296 at all three tide stations in southern Taiwan with an amplitude sign of a trough wave. The travel times of
297 the initial wave to all the stations were recorded: 16 min to Houbihu, 28 min to Dongkung, and 52 min to
298 Kaohsiung. The initial wave was recorded as -0.12 m in Houbihu, -0.09 m in Dongkung, and 0.06 m in
299 Kaohsiung. Following the trough sign of the initial wave, the first wave crest record at Houbihu was 0.3 m,

300 which was approximately 3 times greater than that at Dongkung and 4 times larger than that at Kaohsiung.
301 This was natural because Houbihu was the station closest to the epicentral region and therefore had an
302 earlier arrival time and was relatively sensitive to the surface elevation change in sea level that was induced
303 by the tsunami. The maximum wave heights were recorded as 0.08 m (Kaohsiung), 0.12 m (Dongkung),
304 and 0.3 m (Houbihu). In Kaohsiung and Dongkung, the maximum height was not recorded for the initial
305 wave. The maximum wave height appeared 36 min after the initial wave arrived at Kaohsiung and after 24
306 min at Dongkung, indicating a pattern of wave amplification at these stations. These results suggest that
307 different propagation effects existed at these coastal sites during the passage of the 2006 tsunami. In
308 addition to significant differences in wave amplitude and arrival time, the tsunami records at each station
309 also varied in terms of visible wave periods. The visible period of the tsunami wave at Kaohsiung was
310 recorded from 30-48 min based on the tsunami waveform, which was approximately two times longer than
311 those observed at Dongkung and Houbihu (from 18-24 min). This indicated that wave components with
312 shorter periods were not well recorded in Kaohsiung. The locations and details of the tide gauge
313 observations are summarized in Table 6a for wave amplitude and Table 6b for arrival time and visible period.
314

315 **3.2 Tsunami durations**

316 Another issue was to determine the tsunami duration at each station because it can help to identify the
317 length of wave oscillations at a coastal site due to the tsunami. Typically, the tsunami duration describes the
318 elapsed time during which a high-energy wave at a tide gauge station exceeds the mean sea level of a normal
319 oscillation. The normal oscillation was defined as the site-specific oscillation at each station before the
320 tsunami arrived. RMS analysis was applied to the recorded sea level data at each station. The results of the
321 RMS analysis are plotted in diagrams shown in Figure 9b.

322 The RMS Sea level diagram illustrates how long the high-energy wave persisted at each station.
323 Accordingly, the tsunami duration was determined through a comparison of the RMS sea level and the basic
324 oscillation in sea level at each station. The maximum RMS sea level derived at the Houbihu station was
325 estimated to be 2-3 times higher than those at the Dongkung and Kaohsiung stations. The calculated tsunami
326 duration at Dongkung was as much as 3.9 h, while the tsunami continued for more than 6 h in Kaohsiung
327 and Houbihu.

328 Generally, several oscillation modes are expected to be induced during a tsunami event in association
329 with the tsunami source, propagation path, and topographic effects (Rabinovich, 1997; Rabinovich et al.,
330 2013). An island setting such as Taiwan, where insular shelves and gentle slopes exist, commonly traps
331 waves over the shelf during the passage of tsunamis (Roeber et al., 2009). The trapped waves propagate
332 along the coastline and normally trigger various oscillation modes in the coastal water due to the
333 interference of wave reflection at the edge of the continental shelves (Yamazaki et al., 2011). The wave
334 resonance of these oscillation modes with the fundamental modes of the continental shelf can enhance
335 coastal hazards with amplified amplitudes and long tsunami durations (Wang et al., 2020). The triggered

336 oscillation modes are expected to be mixed with the tsunami source spectrum in the observation records
337 from the coastal sites. To identify these modes from the tsunami source spectrum, spectral analyses were
338 performed on the observation records at all three tide gauge stations in southern Taiwan, as detailed in the
339 next section.

340

341 **4. Spectral analysis**

342 **4.1 Tsunami source spectra**

343 To examine the spectral characteristics of the tsunami waves, Fourier analysis was applied to 10 h of de-
344 tided observed data (i.e., 5 h before and after the tsunami's arrival) that was recorded at all the tide gauge
345 stations in southern Taiwan. The background spectra were calculated in addition to the spectra of the
346 observed tsunami waveform to identify the tsunami effect. The background spectra were the spectral
347 components calculated from observed data 5 h before the tsunami's arrival, and the spectral components of
348 the observed tsunami waveform were computed using the 5 h of data recorded at the tide gauge after the
349 tsunami wave arrived. Figure 10 shows the respective spectra of the observed tsunami waveform and
350 background signals at each tide gauge station.

351 At all the stations, the spectral peaks of the observed tsunami spectra were estimated to be different from
352 those of the background spectra. A visible gap also appeared in the spectral energy between the observed
353 tsunami and the background spectra, revealing the energy generated by the arrival of tsunami waves. To
354 examine the spectral components induced by the arrival of the tsunami waves, the spectral ratio of the
355 observed tsunami and background spectra was derived using equation (10):

$$S_{tsunami}(\omega) = \frac{S_{obs}(\omega)}{S_{bg}(\omega)} \quad (10)$$

356

357 In this equation, $S_{obs}(\omega)$ is the spectral component of the observed tsunami waveform, $S_{bg}(\omega)$ is the
358 background spectrum, and $S_{tsunami}(\omega)$ is the spectral component induced by the arrival of the tsunami waves.
359 Figure 11 shows the spectral ratios for the tsunami spectra at all the stations. Equation (6) assumes
360 equivalent background spectra before and after the tsunami's arrival, indicating that there was no large
361 change in the coastal topography during the tsunami event. Although many earlier studies have reported
362 that coastal topography might be largely changed during a massive tsunami event (e.g., Sugawara, 2018;
363 Masaya et al., 2020), this was not the case for the 2006 tsunami because the tsunami wave was small.
364 Therefore, the dominant peaks of the spectral ratio were connected to either the tsunami source or perhaps
365 the wave oscillation induced by the nonsource phenomenon.

366 Tsunami source periods are periodic components that primarily appear in coastal observations close to
367 the tsunami source region (Toguchi, 2018; Rabinovich, 1977). Accordingly, the tsunami source periods can
368 be estimated from the mean of the spectral ratios calculated from all three stations (i.e., the solid black line
369 shown in Figure 11). From the analysis result of the spectral ratio, the periods of 13.6 min, 16.7 min, and

370 23.1 min are distinct in comparison to other periodic components. The periods within this band most likely
371 presented the source periods of the 2006 tsunami since the periodic components within this band were
372 mostly visible at all stations.

373 In general, a larger earthquake can ordinarily generate a larger tsunami wave with a longer period. For
374 instance, the major periods of the 2011 Tohoku-Oki earthquake tsunami were reported to be 37-67 min in
375 association with that magnitude M_w 9.0 earthquake (Heidarzadeh and Satake, 2013), while shorter dominant
376 periods of 10-22 min were found for the 2013 Santa Cruz tsunami, a M_w 8.0 earthquake (Heidarzadeh,
377 2016). According to the theory introduced by Rabinovich (1997), the approximate dimensions of fault
378 rupture can be estimated from the source periods using the empirical formula defined in equation (11):

$$L = \frac{T}{2} \sqrt{gh} \quad (11)$$

379
380 where g stands for the gravitational acceleration and is set to a constant value of 9.81 m s^{-2} , h represents the
381 seafloor depth around the tsunami source region, L denotes the fault rupture dimensions of length or width,
382 and T is the source period. The approximate source region could be illustrated based on the aftershock
383 distribution one day after the first earthquake occurred. Assuming that the sea depths around the tsunami
384 source region range from 0-600 m and the source periods are 13.6 min, 16.7 min, 20.0 min, and 23.1 min,
385 the relationship between the fault rupture dimensions and sea depths can be derived from equation (3). The
386 correlation derived from equation (11) is plotted in Figure 12.

387 Assuming that the mean sea depth around the tsunami source region is 300 m, the fault rupture
388 dimensions for the two earthquakes can be estimated to be 20-40 km. The approximate fault size of these
389 two earthquakes was estimated to be 800 km^2 , where a longer dimension of 40 km was considered the fault
390 length and 20 km was considered the fault width. The estimation of fault size was fairly consistent with the
391 results derived from the empirical scaling relations of Papazachos et al. (2004), with findings of 794 km^2
392 in association with the M_w 7.0 normal fault earthquake (first earthquake) and 738 km^2 in association with
393 the M_w 6.9 strike-slip fault (second earthquake).

394

395 **4.2 Resonance modes induced by tsunami trapping waves**

396 In addition to the Fourier analyses, wavelet (time-frequency) analyses were also applied to 15 h of de-
397 tided observed data (i.e., from 15:00 on 26 December 2006 to 6:00 on 27 December 2006, Taiwan Standard
398 Time) at all the stations. Wavelet analyses are commonly employed as a method to examine periodic
399 variations over time series through the distribution of tsunami spectral energy. Figure 13 shows the tsunami
400 wavelets derived from the tsunami records observed at each station. According to the wavelet plots at all
401 the stations, period bands of 13.6-23.1 min were clearly recorded after the first wave arrived at all the
402 stations. This also confirmed that the period bands of 13.6-23.1 min were associated with the source periods.
403 At Kaohsiung, the tsunami energy became apparent with periods of 16 min and 36 min approximately 3 h

404 after the arrival of the first wave. In the period channel of 16 min, the oscillation was preserved for
405 approximately 5 h, while the 36 min channel was occupied by a high-energy wave for more than 9 h. At
406 Houbihu, more energy was channeled than at other stations in the period bands of 13.6-23.1 min soon after
407 the first earthquake. This was reasonable because Houbihu was the closest station to the epicentral region
408 and was therefore considered to be more sensitive to the tsunami source than were the other stations.
409 Following the arrival of the first wave, the persistent oscillation (i.e., lasting more than 4 h) was visible
410 approximately 2 h after the first earthquake in the period channels of 16 min, 16.4 min, 20 min, 22.5 min,
411 25.7 min, 30 min, 36 min, and 60 min. These periodic components were considered as possible modes of
412 trapped tsunami waves resonating within the shelf since the wave resonance commonly requires some time
413 to be formed (Heidarzadeh et al., 2021). Among these periods, the 16 min and 36 min periods most likely
414 presented the resonance mode since that mode is visible at only the Kaohsiung and Houbihu stations, where
415 tsunami durations of more than 6 h were recorded (Figure 9b.). From the wavelet analysis of the observed
416 data recorded at the tide gauge stations, the persisting wave oscillations at the Kaohsiung and Houbihu
417 stations might be attributed to tsunami resonance.

418

419 **5. Sensitivity analyses of source models and bathymetry data**

420 **5.1 Single fault models**

421 **5.1.1 Tsunami sensitivity to fault depths**

422 The sensitivity of simulated tsunami waveforms to fault depth was evaluated by varying the central fault
423 depths of the first earthquake. Fault dimensions of 40 km × 20 km were applied to the two earthquakes.
424 The single fault model of the two earthquakes was constructed using the GCMT solution of nodal plane
425 NP2 for the first earthquake and NP1 for the second earthquake. The tide gauge stations of Dongkung and
426 Houbihu were chosen for this sensitivity analysis because they the closest stations to the source region and
427 were therefore more sensitive to the tsunami source. The single fault models of the two earthquakes and the
428 locations of the near-field tide gauge stations that were used for the sensitivity analysis of fault depths are
429 shown in Figure 14a.

430 Figure 14b shows the observed and simulated tsunami waveforms at the Dongkung and Houbihu stations
431 using different fault depths of the first earthquake. At the Dongkung station, the first circle of simulated
432 tsunami waveforms matched the observed data well regardless of the fault depths. At the Houbihu station,
433 the first wave crest of the simulated waveform from a fault depth of 35 km was half the size of the observed
434 value. Simulated tsunami waveforms with shallower depths of 15 km and 20 km produced significantly
435 higher amplitudes during the arrival of the first crest wave. These results revealed that coastal sites with a
436 shorter distance to the source are more sensitive to earthquake fault depths. The simulated waveforms from
437 a central fault depth of 20 km fit the observed data better than other simulations did, and therefore, this was
438 considered the best fault depth for simulation.

439

440 **5.1.2 Comparison of eight models**

441 Single fault models with fault dimensions of 40 km × 20 km and central depths of 20 km for the
442 first earthquake and 33 km for the second earthquake were used in tsunami simulations using eight different
443 sets of focal mechanisms for the two earthquakes estimated from GCMT and USGS data. The single fault
444 models of the two earthquakes with different focal mechanisms are plotted in Figures 15 and 16. The details
445 of the eight different sets of earthquake focal mechanisms are listed in Table 7.

446 In general, the simulated tsunami waveforms from all eight sets of earthquake focal mechanisms
447 matched the observed data well. Figure 17 shows the observed and simulated tsunami waveforms at the
448 Dongkung and Houbihu stations using the eight different sets of earthquake focal mechanisms. The
449 simulated tsunami waveform from the earthquake focal mechanisms of S3 (misfit = 0.530), S5 (misfit =
450 0.529), and S7 (misfit = 0.493) showed a better fit to the observations than did the other simulations (Table
451 7). Among them, the earthquake focal mechanisms of S7 were found to be the best fitting scenario with the
452 smallest misfit from the observations. Scenario S7 contained the fault orientations of NP2 for the first
453 earthquake and NP1 for the second earthquake from USGS's moment tensor solution (Figures 15d, 16c).

454 While the single fault models can produce simulated tsunami waveforms that are consistent with the
455 observations, the poorly sampled (i.e., 6 min interval) signals recorded at the coastal stations also raised
456 some questions, as one would expect some potential high tsunami waves behind the observed signals. To
457 that sense, overestimation of the modeled results was expected, but the simulated tsunami waveforms using
458 single fault models presented the opposite results. This indicates that the single fault models (i.e., with
459 uniform fault slip) may not be sufficient and that the asperity area (i.e., with a large fault slip) on the fault
460 should be evaluated. The tsunami sensitivity to asperity locations of multiple fault models are discussed in
461 the next section.

462

463 **5.2 Tsunami sensitivity to uniform and non-uniform fault slip models**

464 The sensitivity of simulated tsunami waveforms to non-uniform fault slip distribution (i.e., multiple fault
465 model) was evaluated based on the best fitting fault geometry of S7. The fault model with uniform fault
466 slip (i.e., single fault model) was also modeled to identify the significant differences in the modeled results
467 from the uniform and non-uniform slip fault models.

468 Figure 18 shows the observed and simulated tsunami waveforms at the Dongkung and Houbihu stations
469 using non-uniform slip models (LS1-LS9) and a uniform slip model (S7). At the Dongkung station, the
470 simulated tsunami waveforms from non-uniform slip models were not much different from those of the
471 uniform slip models. Both models could produce tsunami waveforms in good agreement with the observed
472 values recorded at this station. At the Houbihu station, the non-uniform slip models produced a significantly
473 higher first wave crest than the observations. The simulated wave peaks from the non-uniform slip models
474 produced wave heights approximately twice those simulated using the uniform slip. These results indicated
475 that the near-field station of Houbihu was rather sensitive to the effect of the fault slip distribution, and

476 some high tsunami waves might have been missing from the recorded signals at the Houbihu station during
477 the 2006 tsunami.

478

479 **5.3 Tsunami simulation using open-source bathymetric data**

480 To analyze the tsunami sensitivity on different sources of open-source, accessible bathymetry data,
481 numerical simulations were applied using GEBCO and ETOPO1 data. The differences between the modeled
482 results using these different bathymetry data were evaluated to compare the modeled wave peaks and
483 waveforms in the 2006 tsunami.

484 Figures 19a and 19b show the spatial distribution of the maximum wave heights simulated using two
485 bathymetric grids, the GEBCO data and ETOPO1 data. To evaluate the differences between the modeled
486 wave peaks, the variation and percent change in the variation were calculated, which can be defined in
487 equations (12) and (13):

$$488 \quad Var_{peak} = Peak_{GEBCO} - Peak_{ETOPO1} \quad (12)$$

$$489 \quad \% Var_{peak} = \frac{Peak_{GEBCO} - Peak_{ETOPO1}}{Peak_{GEBCO}} \times 100 \quad (13)$$

490 where Var_{peak} is the variation in the modeled wave peaks calculated at each computational grid with
491 GEBCO and ETOPO1 data and $Peak_{GEBCO}$ and $Peak_{ETOPO1}$ are defined as the calculated wave peaks
492 of progressive waves in a unit area of the free surface. Figures 19c and 19d illustrate the spatial distribution
493 of the variation and percent change in the variation of the modeled wave peaks in the model domain,
494 indicating the differences in the modeled results using the two bathymetries. The results suggested that the
495 variation in the modeled wave peaks using the two bathymetries was greater than 0.05 m and the percent
496 change was greater than 50% between the modeled results for areas with sea depths of less than 500 m.

497 Figure 20 shows the modeled tsunami waveforms at the three coastal stations (i.e., black circles in Figure
498 19) using the two bathymetric grids. At Kaohsiung, the modeled waveforms from the two bathymetries
499 matched each other well; however, the modeled wave peak from the ETOPO1 data was significantly smaller
500 than that from the GEBCO data. The bathymetries from the GEBCO and ETOPO1 data could produce
501 tsunami waveforms at Dongkung and Houbihu that were similar in both wave periods and peaks. Table 8
502 summarizes the details of the coastal stations and the peak variation percentage of the modeled tsunami
503 waveforms from the two bathymetries.

502

503 **6. The mechanism of tsunami wave trapping**

504 **6.1 Bathymetry effect on tsunami wave directivity**

505 It is commonly understood that tsunami velocities are mainly governed by seafloor depths. A tsunami
506 propagates at a slower speed when the tsunami wave enters shallow water from deeper water. The
507 significant change in propagation speed allows the tsunami to change its wave direction. To assess the

508 bathymetry effect on tsunami wave directivity during propagation, simulations were applied using actual
509 (MS) and manipulated bathymetry experiments (EXP1 and EXP2).

510 Simulated snapshots of tsunami wave propagation using actual (MS) bathymetry data are shown in
511 Figure 21. The continental shelves in front of Hengchun Peninsula have shallow depths compared to the
512 open ocean. Figures 21a and b present how tsunami waves repeatedly changed their directions among the
513 shelves and then refracted into the west coast embayment. The tsunami waves were reflected from the coast
514 after arrival and tended to radiate offshore. However, they did not fully radiate offshore; instead, they were
515 reflected again at the boundary of the shelf and refracted north toward Kaohsiung and Dongkung (Figure
516 21c, d). The high-energy waves repeatedly reflected and refracted among the shelves. Only rare tsunamis
517 were transmitted back to the open ocean or to the east coast. These results indicated that the tsunami waves
518 were trapped over the shelves during their passage in the 2006 tsunami event. Due to this fluctuation, the
519 high-energy tsunami wave remained along the western coast for a long time, which could be clearly seen
520 at 75 min and 90 min after the occurrence of the first earthquake (Figure 21e, f).

521 Figure 22 shows snapshots of the simulated tsunami wave propagation using manipulated (EXP1)
522 bathymetry. In this situation, the transmission of tsunami waves in the shallow area was similar to those
523 simulated using the actual (MS) bathymetry, in which the tsunami waves were persistent and repeatedly
524 reflected and refracted among the shelves, but more reflected waves from the coast radiated to the open sea
525 (Figure 22b-f). This is because the tsunami source was located in an area with sea depths over 500 m, and
526 bathymetry data with sea depths over 500 m were replaced with a 500 m depth in this hypothetical situation.

527 Aside from the numerical experiment EXP1, a rather hypothetical situation (EXP2) was conducted to
528 simulate tsunami wave propagation on a bathymetry with a flat sea bottom and a sea depth of 500 m. Figure
529 23 shows snapshots of simulated tsunami wave propagation using the manipulated (EXP2) bathymetry. An
530 inspection of the tsunami wave transmission in the shallow area indicated that the reflected tsunami waves
531 from the coast radiated homogeneously offshore, and the wave reflection and refraction could not be clearly
532 seen. In addition, the tsunami waves propagated at a rather fast speed (i.e., in comparison to MS and EXP1)
533 and mostly radiated out of the model domain at 75 min and 90 min after the occurrence of the first
534 earthquake (Figure 23 d, e).

535

536 **6.2 Tsunami wave energy trapped on the shelf**

537 While the past section specified that tsunami waves are trapped over shelves due to the wave directivity
538 change associated with the configuration of coastal bathymetry, the question remains of how much wave
539 energy can be trapped over the shelves in front of southern Taiwan during the passage of tsunamis. To
540 quantitatively evaluate the wave energy trapped over the shelves, the trapped ratio was used to indicate the
541 tsunami energy trapped in bathymetric situations, as calculated in equation (14):

$$R_T = \frac{E_{Shelf}}{E_{Total}} \times 100 \quad (14)$$

542 where R_T is the ratio of tsunami energy trapped, E_{Shelf} is the calculated tsunami potential energy on the
 543 shelves (i.e., shallow areas with sea depths under 500 m), and E_{Total} is the calculated total tsunami
 544 potential energy of the model domain at each time step. The tsunami potential energy was determined
 545 assuming that the energy flux of the tsunami wave progressed in a unit region of the free sea surface (Nosov
 546 et al., 2014) and was determined using equation (15):

$$E_p = \iint \frac{1}{2} \rho g \eta^2 dx dy \quad (15)$$

547 where E_p is the tsunami potential energy, ρ is the water density of the ocean, g is the gravitational
 548 acceleration (set as 9.81 m s^{-2}), and η represents the surface integral of the ocean surface disturbance at
 549 each time step. The ratio of trapped tsunami energy was calculated from the snapshots of tsunami
 550 simulations using actual (MS) and manipulated (EXP1 and EXP2) bathymetry. Figure 24 shows the
 551 calculated trapped ratio from simulated tsunami propagation snapshots every 15 min using actual (MS) and
 552 manipulated (EXP1 and EXP2) bathymetry. Note that for calculating the trapped ratio from simulations
 553 using manipulated bathymetry (EXP1 and EXP2), the shelf region corresponding to the actual bathymetry
 554 (MS) was used (i.e., the shallow area illustrated by the solid and dashed black lines shown in Figures 22
 555 and 23). According to equations (14) and (15), the simulations yielded a ratio of trapped tsunami energy of
 556 more than 50% when using actual bathymetry (MS) and manipulated bathymetry (EXP1) but a smaller
 557 trapped ratio of 20% when using manipulated bathymetry (EXP2). These results quantitatively provided
 558 confirmation that the coastally trapped tsunami wave energy was related to the shape of the bathymetry.

559

560 **6.3 Comparison of simulated tsunami waveforms**

561 To understand any significant change in tsunami waveforms that can be recognized with and without
 562 wave trapping, tsunami waveforms simulated from actual (MS) and manipulated bathymetry (EXP1 and
 563 EXP2) were compared. Figure 25 shows the simulated tsunami waveforms at the three coastal stations in
 564 southern Taiwan using actual and manipulated bathymetry.

565 Using the manipulated bathymetry (EXP1), the first few circles of simulated tsunami waveforms at all
 566 the stations were consistent with those simulated using actual bathymetry (MS) but produced slightly
 567 smaller later phase amplitudes. An inspection of the simulated waveforms using the manipulated
 568 bathymetry (EXP2) indicated an earlier arrival time of the first wave and smaller amplitudes of the later
 569 phase than those of the simulation results using actual (MS) bathymetry. These results indicated that the
 570 persistent high-energy waves along the south coast of Taiwan were associated with the mechanism of
 571 tsunami wave trapping.

572

573 **6.4 Amplified and persistent high-energy waves along the coast**

574 As described in the previous sections, the tsunami wave was trapped over the shelves and transmitted
 575 along the coast as edge waves during the 2006 tsunami. This section describes how tsunami waves behave

576 as edge waves and to what extent such wave fluctuations influence the amplified and persisting high-energy
577 waves along the south coast of Taiwan. Figure 26 shows the shelves in front of south Taiwan and the
578 simulated tsunami heights of the 2006 tsunami from the main simulation (MS).

579 To study the behaviors of edge waves along the south coast during the 2006 tsunami, a time-distance
580 diagram of tsunami waves is shown. Figure 27a shows the time-distance diagram of the tsunami wave along
581 the contour of the 20 m sea depth (i.e., dashed black line in Figure 26a). Based on the phase shift of the
582 tsunami wave, the propagation path and the travel time curve of edge waves were illustrated (i.e., green
583 arrow in Figure 27a). According to the travel time curve, the edge waves propagated along the coast at a
584 speed of 50 m s^{-1} . The edge waves propagated along the coast and were iteratively reflected at the shelf
585 edge. The coupling of the edge waves and the later-arriving incident waves amplified the tsunami waves
586 and maintained the wave oscillation in the later phase. These were visible from simulated tsunami
587 waveforms at numerical wave gauges C and E, as shown in Figure 27c.

588 To understand the persisting high-energy waves along the south coast of Taiwan during the 2006 tsunami,
589 the decreasing tendency of the tsunami wave energy along the 20 m sea depth contour was analyzed. The
590 temporal tsunami wave energy was first determined using equation (11) and then normalized according to
591 the maximum temporal tsunami energy in the time series. Figure 27b shows the time-distance diagram of
592 the normalized tsunami energy along the 20 m sea depth contour (i.e., dashed black line in Figure 26a).
593 Figure 27d shows the normalized tsunami energy at numerical wave gauges C and E. At the numerical wave
594 gauge C, the normalized tsunami energy achieved its greatest value at approximately 40 min after the first
595 earthquake occurred. However, this high-energy channel did not decrease with time after the first wave
596 arrived; instead, a persisting channel of strong energy was visible. This energy channel lasted for more than
597 60 min, and the wave energy repeatedly reached the maximum value in this channel. Beyond this channel,
598 the energy commenced to decrease with a rate of energy loss of 50% at 110 min and 20% at 270 min after
599 the occurrence time of the first earthquake. At the numerical wave gauge E, the normalized tsunami energy
600 achieved its greatest value approximately 30 min and 120 min after the first wave arrived. Beyond this
601 channel, the energy commenced to decrease at a rather fast rate of energy loss of 80% at 150 min and 70%
602 at 215 min after the occurrence time of the first earthquake. Accordingly, the tsunami decay process in this
603 region was expected to last for more than 300 min. These results indicated that the wave amplification and
604 persistent high-energy waves along the coast during the 2006 tsunami were connected to tsunami wave
605 trapping and the influence of edge waves. According to these behaviors, southern Taiwan could be affected
606 by intensified coastal hazards and severe impacts from tsunamis.

607

608 **7. Conclusions**

609 **7.1 Main findings**

610 In this article, the characteristics of the consecutive tsunamis on 26 December 2006 and the resulting
611 tsunami behaviors in southern Taiwan were investigated and clarified. The methodology comprised

612 analyses of tide gauge tsunami waveforms, spectral analyses and numerical tsunami simulations. The main
613 findings are summarized as follows:

614 (1) The physical characteristics of the tsunami waveforms at all three tide gauge stations in southern
615 Taiwan during the December 2006 tsunami were analyzed. The initial tsunami wave arrived at
616 Kaohsiung, Dongkung, and Houbihu at 21:18, 20:54, and 20:42 Taiwan Standard Time, respectively,
617 with a trough sign of tsunami amplitude. Following the initial wave trough, the initial wave crests were
618 0.07 m (Kaohsiung), 0.09 m (Dongkung), and 0.3 m (Houbihu). The maximum tsunami wave heights
619 at the three tide gauge stations at Kaohsiung, Dongkung, and Houbihu were 0.08 m, 0.12 m, and 0.3
620 m, respectively, and the maximum tsunami wave heights at Kaohsiung and Dongkung were not
621 recorded with the first arrivals. The approximate tsunami duration in Dongkung was 3.9 h, while the
622 tsunami lasted for more than 6 h in Kaohsiung and Houbihu.

623 (2) Based on the spectral analyses of tsunami waveforms, a period band of 13.6-23.1 min was attributed
624 to the tsunami source spectrum. The periods of 16 min and 36 min were considered as the modes of
625 trapped tsunami waves resonating with the fundamental modes of the shelves.

626 (3) A tsunami source model for the 2006 earthquake doublet tsunami was proposed. The fault size of the
627 successive earthquakes was estimated to be 800 km², comprising a length of 40 km and a width of 20
628 km. Uniform slips of 1.66 m (first earthquake, M_w 7.0) and 1.17 m (second earthquake, M_w 6.9) were
629 estimated. The respective central fault depths of the two earthquakes were 20 km and 33 km. The focal
630 mechanisms of the first earthquake, with a strike of 319°, dip of 69°, and rake of -102°, and the second
631 earthquake, with a strike of 151°, dip of 48°, and rake of 0°, could successfully produce the observed
632 tsunami waveforms. Moreover, the tsunami sensitivity of the non-uniform fault slip distribution
633 indicated that some tsunami signals might have been missing from the record signals due to the poor
634 sampling rate (6 min intervals), and the wave peaks at Houbihu station might have reached twice the
635 values of those observed during the 2006 tsunami.

636 (4) A comparison of tsunami propagation simulations using actual (MS) and manipulated bathymetry
637 (EXP1 and EXP2) revealed that the tsunami waves were coastally trapped during the passage of the
638 2006 tsunami. The trapped tsunami waves iteratively reflected and refracted among the shelves. The
639 trapped waves interfered with incident waves and resonated with the fundamental modes of the shelves,
640 resulting in an amplified and persistent oscillation of tsunami waves. This explained why the observed
641 tsunami waves recorded at some stations in southern Taiwan were amplified and had a tsunami duration
642 of more than 6 h during the 2006 tsunami.

643 (5) Tsunamis are one of the most dangerous coastal hazards and can cause destructive damage and loss of
644 life in coastal regions. Taiwan is at risk of tsunamis and is exposed to potential near-field tsunamis
645 generated from the Manila Trench on the South China Sea (SCS) side and the Ryukyu Trench on the
646 Pacific Ocean side. The results of the present study based on the 2006 tsunami revealed that the tsunami
647 wave was trapped over the insular shelves around southern Taiwan during the passage of the tsunami.

648 Wave couplings and resonant features might result in unexpected amplification of tsunami heights and
649 persistent wave oscillation in southern Taiwan. In other words, even if the initial wave heights are small,
650 the tsunami waves that arrive later are expected to be higher and more persistent along the coast of
651 southern Taiwan. Therefore, decision makers and people in southern Taiwan should be aware of this
652 possibility and stay clear of coastal regions for a long time as an emergency response to future tsunamis,
653 even if the wave height of an initially arriving tsunami wave is small. These findings are important and
654 valuable for improving the existing system of tsunami warnings and coastal planning for disaster risk
655 management.

656

657 **7.2 Limitations and future improvements**

658 In this study, the characteristics of the December 2006 tsunami and resulting tsunami behaviors in
659 southern Taiwan were explored using available data from tide gauge tsunami waveforms and numerical
660 tsunami simulations. Nevertheless, the analyses in this article had some limitations. The first limitation was
661 related to the tsunami data recorded at the tide gauge stations, which were employed as input data for the
662 spectral analyses (i.e., Fourier analyses and wavelet analyses) and compared with the numerical results.
663 The sampling interval of the tide gauge data recorded at all CWB tide gauge stations was 6 min, indicating
664 that tsunami wave components with shorter periods might not be well recorded in the tide gauge data. Due
665 to this existing limitation, spectral analyses might cause discrepancies in detecting periodic components of
666 tsunami spectra. This limitation could be improved by including tsunami data with more frequent sampling
667 rates.

668 Another limitation was related to the simulation grid size (i.e., 450 m) for the tsunami propagation
669 simulation. Although the simulated tsunami waveforms were reasonably consistent with the observed
670 values recorded at the tide gauge stations in terms of wave amplitude and arrival time, the reproducibility
671 of the numerical results for the 2006 tsunami could be further improved by constructing a finer grid of
672 bathymetric data.

673 All the limitations mentioned above suggest further improvements to research to provide a more detailed
674 investigation of long-lived edge wave and shelf resonance issues, especially in the region of southern
675 Taiwan. In addition, more fundamental studies on the complex wave mechanisms of tsunami reflection and
676 refraction, shoaling effects, and wave trapping by insular shelves are planned for future work.

677

678 *Code availability.* The second version of TUNAMI code (TUNAMI-N2) conducted in this research is
679 currently not open-source model but is available from the corresponding author upon reasonable request.

680

681 *Data availability.* The record sea level data at tide gauge stations were obtained from Central Weather
682 Bureau, R.O.C. through reasonable request. The seismic information is available in publicly accessible
683 catalogs of the GCMT Project and USGS, as mentioned in the body of the article. The GEBCO and

684 ETOPO1 bathymetric data used for the numerical tsunami simulations are publicly assessable at
685 <https://www.gebco.net> (General Bathymetric Chart of the Ocean, 2021) and
686 <https://www.ngdc.noaa.gov/mgg/global> (National Oceanic and Atmospheric Administration, 2009).

687

688 *Author contributions.* All authors read, reviewed, and approved the manuscript. C.A.C wrote the manuscript,
689 performed numerical simulation, and analyzed the results. F.I. and A.S. supervised the research and
690 collected the funding. K.P. provide constructive suggestions to the study and numerical simulation.

691

692 *Competing interests.* All authors declare no competing interest.

693

694 *Acknowledgments.* The authors thank Ms. Shyh-Fang Liu and Ms. Cheng-Lin Huang for their great support
695 in collecting the observation data used in this work. The authors would like to express their sincere
696 appreciation to Dr. Yo Fukutani from Kanto Gakuin University for his valuable suggestions on conducting
697 the sensitivity analysis of the fault models. We appreciated Andy Brandt, PhD, from group of American
698 Journal Expert (<https://www.aje.com>) for editing the draft of the manuscript. This work was supported (in
699 part) by the MEXT WISE Program for Sustainability in the Dynamic Earth.

700

701 **References**

702 Cheng, S., Shaw, C., and Yeh, Y., Reconstructing the 1867 Keelung Earthquake and Tsunami Based on
703 Historical Documents, *Terr. Atmos. Ocean. Sci.*, Vol. 27, No. 3, 431-449, June 2016

704 Earthquake Research Committee, The headquarter of Earthquake Research Promotion: Tsunami prediction
705 method for earthquakes with characterized source faults (Tsunami Recipe) (2017), available at:
706 https://www.jishin.go.jp/main/tsunami-e/17jan_tsunami-recipe.pdf (last access: 14 January 2022)

707 Fukutani, Y., Moriguchi, S., Terada, K., & Otake, Y. (2021). Time-dependent probabilistic tsunami
708 inundation assessment using mode decomposition to assess uncertainty for an earthquake scenario.
709 *Journal of Geophysical Research: Oceans*, 126, e2021JC017250.
710 <https://doi.org/10.1029/2021JC017250>

711 Griffin, J., Latief, H., Kongko, W., Harig, S., Horspool, N., Hanung, R., ... & Cummins, P. (2015). An
712 evaluation of onshore digital elevation models for modeling tsunami inundation zones. *Frontiers in Earth
713 Science*, 3, 32.

714 Gusman, A., Satake, K., Shinohara, M., Sakai, S., Tanioka, Y., Fault Slip Distribution of the 2016
715 Fukushima Earthquake Estimated from Tsunami Waveforms, *Pure Appl. Geophys.*, 174, 2925-2943 (2017)

716 Hayashi, Y., Koshimura, S., and Imamura, F., Comparison of decay features of the 2006 and 2007 Kuril
717 Island earthquake tsunamis, *Geophys. J. Int.* (2012) 190, 347-357

718 Heidarzadeh, M., and Satake, K., Waveform and spectral analyses of the 2011 Japan tsunami records on
719 tide gauge and DART stations across the Pacific Ocean, *Pure Appl. Geophys.*, 170, 1275–1293,
720 doi:10.1007/s00024-012-0558-5, 2013.

721 Heidarzadeh, M., Harada, T., Satake, K., Ishibe, T., and Gusman, A. R., Comparative study of two
722 tsunamigenic earthquakes in the Solomon Islands: 2015 Mw 7.0 normal-fault and 2013 Santa Cruz Mw 8.0
723 megathrust earthquakes, *Geophys. Res. Lett.*, 43, 4340–4349. doi:10.1002/2016GL068601, 2016.

724 Heidarzadeh, M., Muhari, A., and Wijanarto, A., Insight on the Source of the 28 September 2018 Sulawesi
725 Tsunami, Indonesia Based on Spectral Analyses and Numerical Simulation, *Pure Appl. Geophys.*, 176, 25-
726 43, <https://doi.org/10.1007/s00024-018-2065-9>

727 Harris, C. R., Millman, K. J., van der Walt, S. J., Gommers, R., Virtanen, P., Cournapeau, D., ... Oliphant,
728 T. E. (2020). Array programming with NumPy. *Nature*, 585, 357–362. [https://doi.org/10.1038/s41586-020-](https://doi.org/10.1038/s41586-020-2649-2)
729 2649-2

730 Heidarzadeh, M., Pranantyo, I., Okuwaki, R., Dogan, G., and Yalciner, A., Long Tsunami Oscillations
731 Following the 30 October 2020 Mw7.0 Aegean Sea Earthquake: Observation and Modelling, *Pure Appl.*
732 *Geophys.*, 1531-1548, <https://doi.org/10.1007/s00024-021-02761-8>

733 Imamura, F.: Review of tsunami simulation with a finite difference method, *Long-Wave Runup Models*,
734 World Scientific, 25–42, 1995.

735 Kagan, Y., Y., Jackson, D. D. (1999), Worldwide doublets of large shallow earthquake, *Bulletin of the*
736 *Seismological Society of America*, 89, 5, pp. 1147-1155

737 Koshimura, S., Hayashi, Y., Munemoto, K., & Imamura, F. (2008). Effect of the Emperor seamounts on
738 trans-oceanic propagation of the 2006 Kuril Island earthquake tsunami. *Geophysical Research Letters*,
739 35(2), [L02611]. <https://doi.org/10.1029/2007GL032129>

740 Koyano, K., Takabatake, T., Esteban, M., Shibayama, T., ASCE, M., Influence of Edge Waves on Tsunami
741 Characteristics along Kujukuri Beach, Japan, *Journal of Waterway, Port, Coastal, and Ocean Engineering*,
742 doi: 10.1061/(ASCE)WW.1943-5460.0000617.

743 Lay, T., and Kanamori, H., EARTHQUAKE DOUBLET IN THE SOLOMON ISLANDS, *Physics of the*
744 *Earth and Planetary Interiors*, 21 (1980) 283-304

745 Li, L., A. D. Switzer, Y. Wang, R. Weiss, Q. Qiu, C.-H. Chan, and P. Tapponnier (2015), What caused the
746 mysterious eighteenth century tsunami that struck the southwest Taiwan coast?, *Geophys. Res. Lett.*, 42,
747 8498–8506, doi:10.1002/2015GL065567.

748 Li, L., A. D. Switzer, C.-H. Chan, Y. Wang, R. Weiss, and Q. Qiu (2016), How heterogeneous coseismic
749 slip affects regional probabilistic tsunami hazard assessment: A case study in the South China Sea, *J.*
750 *Geophys. Res. Solid Earth*, 121, 6250–6272, doi:10.1002/2016JB013111.

751 Liu, L., Wang, X., and Salisbury, A., Tsunami hazard and early warning system in South China Sea, *Journal*
752 *of Asian Earth Science*, 36 (2009) 2-12

753 Ma, K., Liang, W., (2008), Preface to the 2006 Pingtung Earthquake Doublet Special Issue, *Terr. Atmos.*
754 *Ocean. Sci.*, Vol. 19, No. 6, I-III, December 2008, doi: 10.3319/TAO.2008.19.6I (PT)

755 Masaya, R., Suppasri, A., Yamashita, K., Imamura, F., Gouramanis, C., and Leelawat, N., Investigating
756 beach erosion related with tsunami sediment transport at Phra Thong Island, Thailand, caused by the 2004
757 Indian Ocean Tsunami, *Nat. Hazards Earth Syst. Sci.*, 20, 2823–2841, 2020, [https://doi.org/10.5194/nhess-](https://doi.org/10.5194/nhess-20-2823-2020)
758 20-2823-2020

759 Megawati, K., Shaw, F., Sieh, K., Huang, Z., Wu, T., Lin, Y., Tan, S., Pan, T., Tsunami hazard from the
760 subduction megathrust of the South China Sea: Part 1. Source characterization and the resulting tsunami,
761 *Journal of Asian Earth Science* 36 (2009) 13-20

762 Okada, Y., Surface deformation due to shear and tensile faults in a half-space, *Bull. Seismol. Soc. Am.*,
763 75(4), 1135–1154, 1985.

764 Okal, E. A., Synolakis, C. E. and Kalligeris, N.: Tsunami simulations for regional sources in the South
765 China and adjoining seas, *Pure. Appl. Geophys.*, 168(6), 1153–1173, doi: 10.1007/s00024-010-0230-x,
766 2011.

767 Otake, T., Chua, C. T., Suppasri, A., Imamura, I., Justification of Possible Casualty-Reduction
768 Countermeasures Based on Global Tsunami Hazard Assessment for Tsunami-Prone Regions over the Past
769 400 Years, *Journal of Disaster Research* Vol. 15 No.4, 2020

770 Papazachos, B., Scordilis, E., Panagiotopoulos, D., Papazachos, C., Karakaisis, G., Global relations
771 between seismic fault parameters and moment magnitude of earthquakes, *Bull. Geol. Soc. Greece XXXVI*
772 (2004) 1482-1489

773 Qiu, Q., Li, L., Hsu, Y., Wang, Y., Chan, C., and Switzer, A., Revised earthquake sources along Manila
774 trench for tsunami hazard assessment in the South China Sea, *Nat. Hazards Earth Syst. Sci.*, 19, 1565–1583,
775 2019 <https://doi.org/10.5194/nhess-19-1565-2019>

776 Rabinovich, A., Spectral analysis of tsunami waves: Separation of the source and topography effects,
777 *JOURNAL OF GEOPHYSICAL RESEARCH*, VOL. 102, NO. C6, PAGES 12,663-12,676, JUNE 15, 1997

778 Rabinovich, A., Candella, R., and Thomson, R., The open ocean energy decay of the three recent trans-
779 Pacific tsunamis, *GEOPHYSICAL RESEARCH LETTERS*, VOL. 40, 3157-3162, doi: 10.2002/grl.50625,
780 2013

781 Roeber, V., Yamazaki, Y., and Cheung, K., Resonance and impact of the 2009 Samoa tsunami around Tutuila,
782 American Samoa, *GEOPHYSICAL RESEARCH LETTERS*, VOL. 37, L21604, doi:
783 10.1029/2010GL044419, 2010

784 Satake, K., Fujii, Y., Harada, T., & Namegaya, Y. (2013). Time and space distribution of coseismic slip of
785 the 2011 Tohoku Earthquake as inferred from tsunami waveform data. *Bulletin of the Seismological Society*
786 *of America*, 103(2B), 1473–1492. <https://doi.org/10.1785/0120120122>

787 Sugawara, D., Yu, N., and Yen, J., Estimating a Tsunami Source by the Sediment Transport Modeling: A
788 Primary Attempt on a Historical/ 1867 Normal-Faulting Tsunami in Northern Taiwan, *Journal of*
789 *Geophysical Research: Earth Surface*, 124, 1675–1700. <https://doi.org/10.1029/2018JF004831>

790 Sun, Y.-S., Chen, P.-F., Chen, C.-C., Lee, Y.-T., Ma, K.-F., and Wu, T.-R.: Assessment of the peak tsunami
791 amplitude associated with a large earthquake occurring along the southernmost Ryukyu subduction zone in
792 the region of Taiwan, *Nat. Hazards Earth Syst. Sci.*, 18, 2081–2092, [https://doi.org/10.5194/nhess-18-2081-](https://doi.org/10.5194/nhess-18-2081-2018)
793 2018, 2018.

794 Sugawara D. (2018) Evolution of Numerical Modeling as a Tool for Predicting Tsunami-Induced
795 Morphological Changes in Coastal Areas: A Review Since the 2011 Tohoku Earthquake. In: Santiago-
796 Fandiño V., Sato S., Maki N., Iuchi K. (eds) *The 2011 Japan Earthquake and Tsunami: Reconstruction and*
797 *Restoration. Advances in Natural and Technological Hazards Research*, vol 47. Springer, Cham.
798 https://doi.org/10.1007/978-3-319-58691-5_26

799 Suppasri, A., Imamura, F., Koshimura, F., EFFECT OF THE RUPTURE VELOCITY OF FAULT MOTION,
800 OCEAN CURRENT AND INITIAL SEA LEVEL ON THE TRANSOCEANIC PROPAGATION OF
801 TSUNAMI, *Coastal Engineering Journal*, Vol. 52, No. 2 (2010) 107-132, Doi:
802 10.1142/S0578563410002142

803 Suppasri, A., Fukutani, T., Tabuchi, S., Imamura, F., Mapping of historical tsunamis in the Indian and
804 Southwest Pacific Oceans, *International Journal of Disaster Risk Reduction*1 (2012) 62-71,

805 Suppasri, A., Muhari, A., Fukutani, T., Imamura, F., and Shuto, N., Loss Functions for Small Marine Vessels
806 Based on Survey Data and Numerical Simulation of the 2011 Great East Japan Tsunami, *Journal of*
807 *Waterway, Port, Coastal, and Ocean Engineering*, doi: 10.1061/(ASCE)WW.1943-5460.0000244

808 Suppasri, A., Leelawat, N., Latcharote, P., Roeber, V., Yamashita, K., Hayashi, A., Ohira, H., Fukui, K.,
809 Hisamatsu, A., Nguyen, David, Imamura, F., The 2016 Fukushima earthquake and tsunami: Local tsunami
810 behavior and recommendations for tsunami disaster risk reduction, *International Journal of Disaster Risk*
811 *Reduction* 21 (2017) 323-330

812 Suppasri, A., Maly, E., Kitamura, M., Syamsidik, Pescaroli. G., Alexander, D., Imamura, F., Cascading
813 disasters triggered by tsunami hazards: A perspective for critical infrastructure resilience and disaster risk
814 reduction, *International Journal of Disaster Risk Reduction*66 (2021) 1002597

815 Tanioka, Y., and Satake, K., Tsunami generation by the horizontal displacement of the ocean bottom,
816 *GEOPHYSICAL RESEARCH LETTERS*, VOL. 23, NO. 8, PAGES 861-864, APRIL 15, 1996

817 Torrence, C., and Compo, G., A practical guide to wavelet analysis, *Bull. Am. Meteorol. Soc.*, 79, 61–78,
818 doi:10.1175/1520-0477(1998)0792.0.CO;2, 1998.

819 Toguchi, Y., Fujii, S., & Hinata, H. (2018), Tsunami waves and tsunami-induced natural oscillations
820 determined by HF radar in Ise Bay, Japan. *Journal of Geophysical Research: Oceans*, 123, 2965–2980.
821 <https://doi.org/10.1029/2017JC013626>

822 Wang, Y., Zamora, N., Quiroz, M., Satake, K., & Cienfuegos, R. (2021). Tsunami resonance
823 characterization in Japan due to trans-Pacific sources: Response on the bay and continental shelf. *Journal*
824 *of Geophysical Research: Oceans*, 126, e2020JC017037. <https://doi.org/10.1029/2020JC017037>

825 Wu, T., and Huang, H., Modeling tsunami hazards from Manila trench to Taiwan, *Journal of Asian Earth*
826 *Science* 36 (2009) 21-78

827 Wu, T., Chen, P., Tsai, W., Chen, G., Numerical Study on Tsunami Excited by 2006 Pingtung Earthquake
828 Doublet, *Terr. Atmos. Ocean. Sci.*, Vol. 19, No. 6, 705-715, December 2008

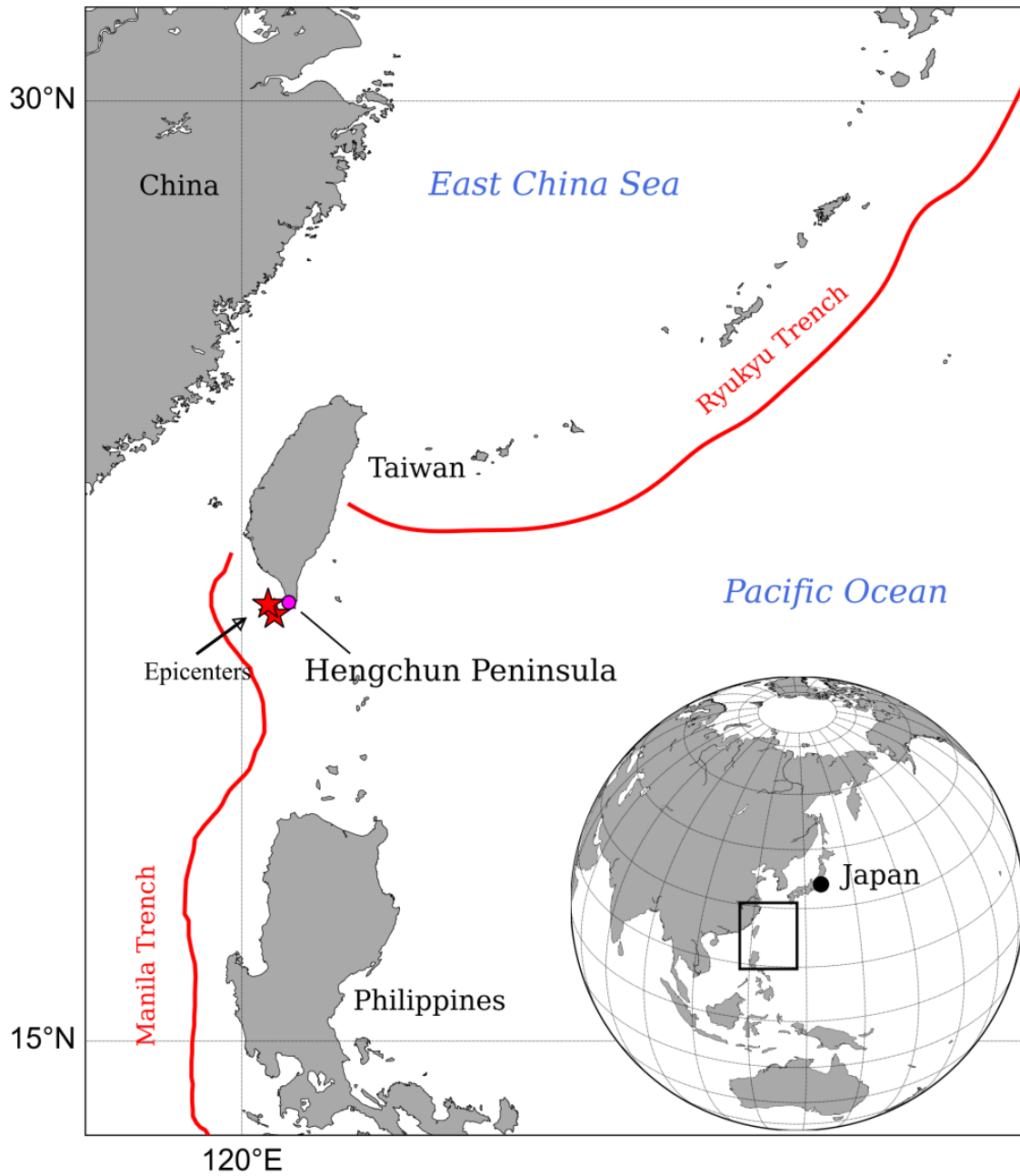
829 Wu, Y., Zhao, L., Chang, C., Hsiao, N., Chen, Y., and Hsu, S., Relocation of the 2006 Pingtung Earthquake
830 sequence and seismotectonics in Southern Taiwan, *Tectonophysics* 479 (2009) 19-27

831 National Disaster Prevention and Protection Commission, R.O.C., 2007. Statistics on the Losses on Natural
832 Disaster. <http://www.ndppc.nat.gov.tw/>.

833 Yamazaki, Y., and Cheung, L., Shelf resonance and impact of near-field tsunami generated by the 2010
834 Chile earthquake, *GEOPHYSICAL RESEARCH LETTERS*, VOL. 38, L12605,
835 doi:10.1029/2011GL047508, 2011

836 Zengaffinen, T., Løvholt, F., Pedersen, G. K., & Muhari, A. (2020). Modelling 2018 Anak Krakatoa Flank
837 Collapse and Tsunami: effect of landslide failure mechanism and dynamics on tsunami generation. *Pure*
838 *and Applied Geophysics*, 177(6), 2493-2516.

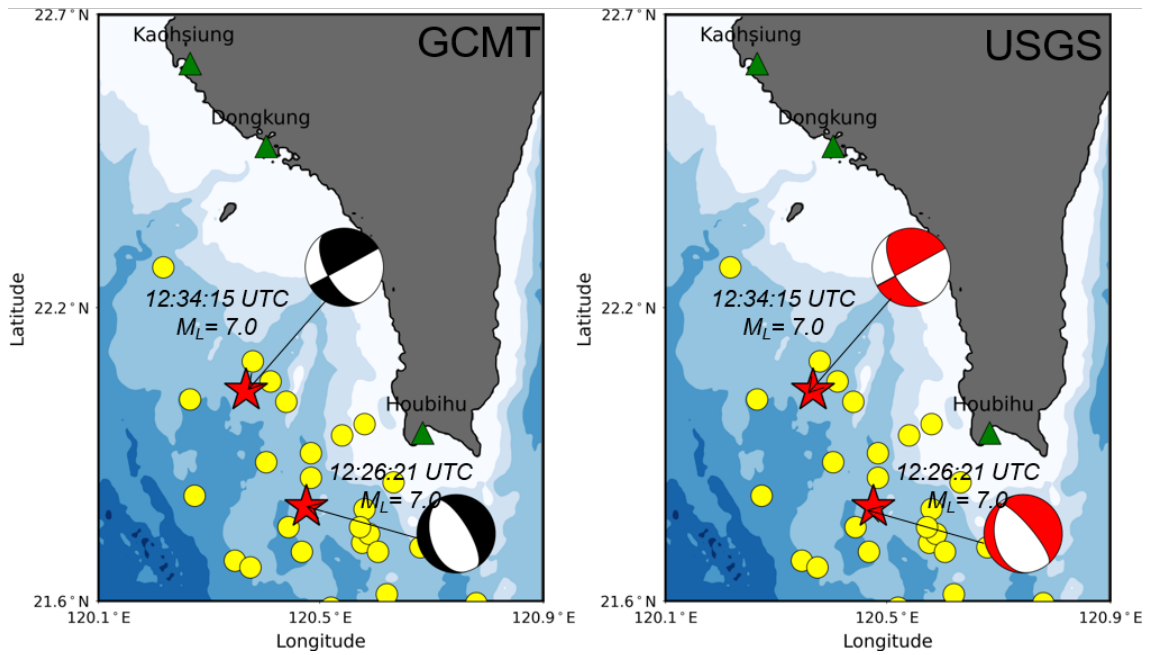
839



840

841 **Figure 1. Map of the Hengchun Peninsula, Taiwan. The red stars illustrate the epicenters of the**
 842 **doublet earthquakes, and the solid red lines illustrate the subduction zones of the Manila Trench**
 843 **and the Ryukyu Trench.**

844



845

846

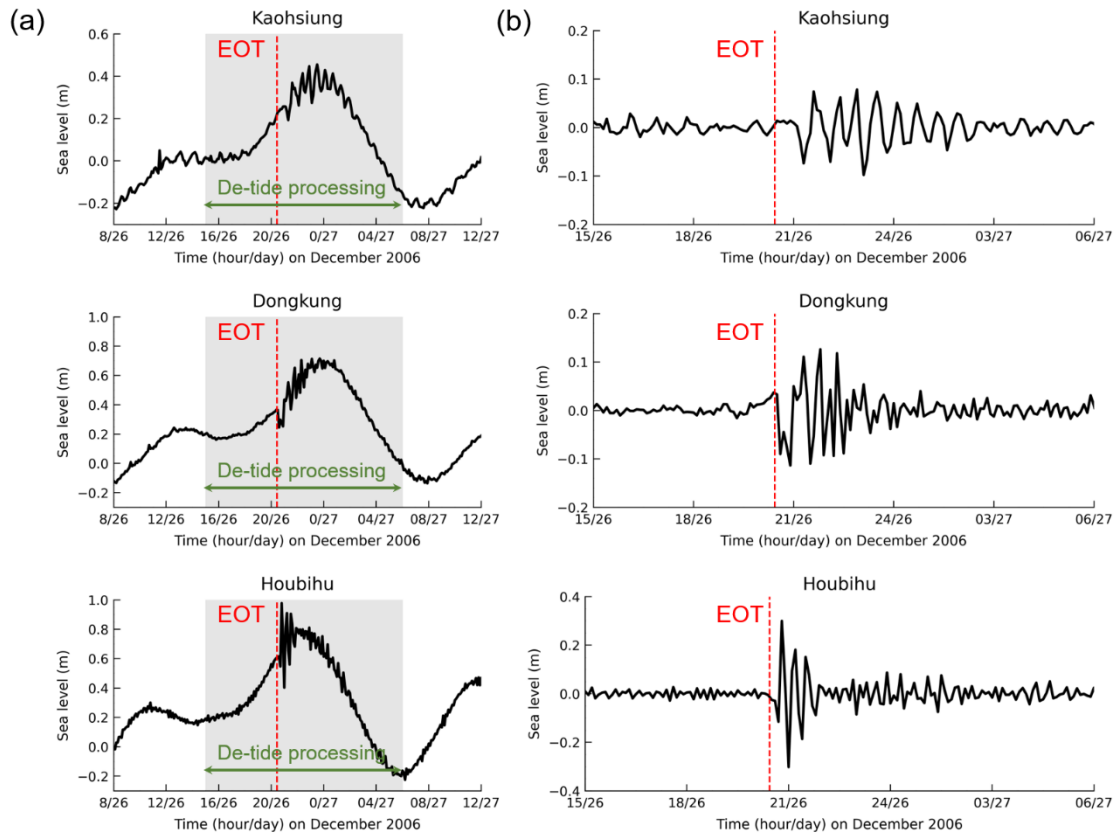
847

848

849

850

Figure 2. The tectonic settings of the 2006 earthquake doublet. The red stars denote the epicenters of the successive earthquakes. The beachballs denote the focal mechanisms of the two earthquakes estimated from the GCMT and USGS moment tensor solutions. The yellow circles show the aftershock distribution for one day from the USGS earthquake catalog. The green triangles represent the locations of the CWB tide gauge stations.



851
 852 **Figure 3. The (a) original and (b) de-tided sea levels recorded at tide gauge stations in southern**
 853 **Taiwan during the 26 December 2006 tsunami event. The vertical, dashed red lines indicate the**
 854 **earthquake occurrence time (EOT). The gray shaded areas illustrate the tide gauge data used**
 855 **for de-tide processing. The data shown in the graphs were drawn based on Taiwan Standard**
 856 **Time.**

857

858

859 **Table 1. Calculation conditions for the numerical tsunami simulation.**

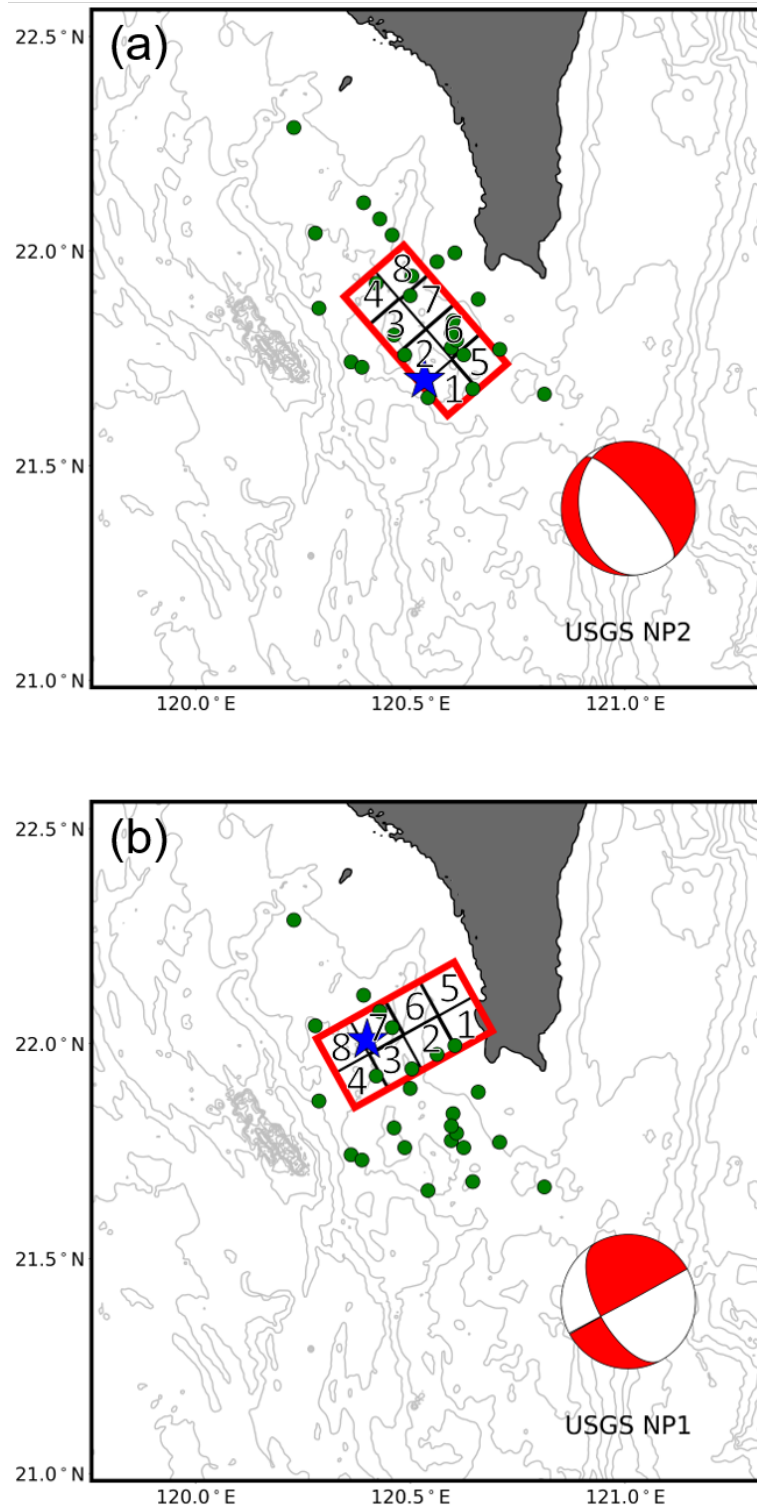
Calculation condition for the numerical tsunami simulation	
Governing equation	Two-dimensional nonlinear shallow water equations (TUNAMI-N2 model)
Numerical integration method	Leap-frog finite difference method
Initial condition	Initial water level calculated from fault parameters using the theory of Okada, 1985 considering the contribution of horizontal coseismic displacement
Coordination system	Cartesian coordinate system
Boundary condition	Radiation boundary condition
Stability criterion	Courant–Friedrichs–Lewy (CFL) condition
Time interval	0.1 s
Mesh size	450 m
Mesh number (x, y)	(538, 631)

860

861

Table 2. Focal mechanisms for successive earthquakes estimated by GCMT and USGS.

		Earthquake 1		Earthquake 2	
		NP1	NP2	NP1	NP2
GCMT	Long (° E)	120.52		120.4	
	Lat (° N)	21.81		22.02	
	Strike (deg)	165	329	151	61
	Dip (deg)	30	61	48	90
	Rake (deg)	-76	-98	0	138
	Depth (km)	20		33	
	USGS	Long (° E)	120.55		120.49
Lat (° N)		21.8		21.97	
Strike (deg)		171	319	151	61
Dip (deg)		24	69	48	90
Rake (deg)		-61	-102	0	138
Depth (km)		25		33	



864
 865
 866
 867
 868

Figure 4. Fault models for the two earthquakes. (a) Subfault locations of the first earthquake (M_w 7.0) using NP2 of USGS's moment tensor solution. (b) Subfault locations of the second earthquake (M_w 6.9) using NP1 of USGS's moment tensor solution.

869

Table 3. Parameters of the subfaults for the two earthquakes of the 2006 earthquake doublet.

	Sub fault	Long (°E)	Lat (°N)	Length (km)	Width (km)	Depth (km)	Strike (°)	Dip (°)	Rake (°)
Earthquake 1	1	120.619	21.588	10	10	15.3	319	69	-102
	2	120.556	21.657	10	10	15.3	319	69	-102
	3	120.492	21.724	10	10	15.3	319	69	-102
	4	120.429	21.792	10	10	15.3	319	69	-102
	5	120.692	21.648	10	10	24.7	319	69	-102
	6	120.629	21.716	10	10	24.7	319	69	-102
	7	120.565	21.784	10	10	24.7	319	69	-102
	8	120.501	21.852	10	10	24.7	319	69	-102
Earthquake 2	1	120.726	21.989	10	10	29.1	151	48	0
	2	120.642	21.946	10	10	29.1	151	48	0
	3	120.557	21.902	10	10	29.1	151	48	0
	4	120.473	21.858	10	10	29.1	151	48	0
	5	120.680	22.068	10	10	29.1	151	48	0
	6	120.595	22.024	10	10	36.5	151	48	0
	7	120.510	21.980	10	10	36.5	151	48	0
	8	120.426	21.936	10	10	36.5	151	48	0

870

871

872 **Table 4a. Details of the average slip, large slip, and background slip for the two earthquakes.**

	Earthquake 1	Earthquake 2
Moment magnitude (M_w)	7.0	6.9
Entire fault size (km^2)	800	800
Rigidity (GPa)	30	30
Average slip D_a (m)	1.66	1.17
Large slip $2D_a$ (m)	3.32	2.35
Background slip (m)	1.11	0.78

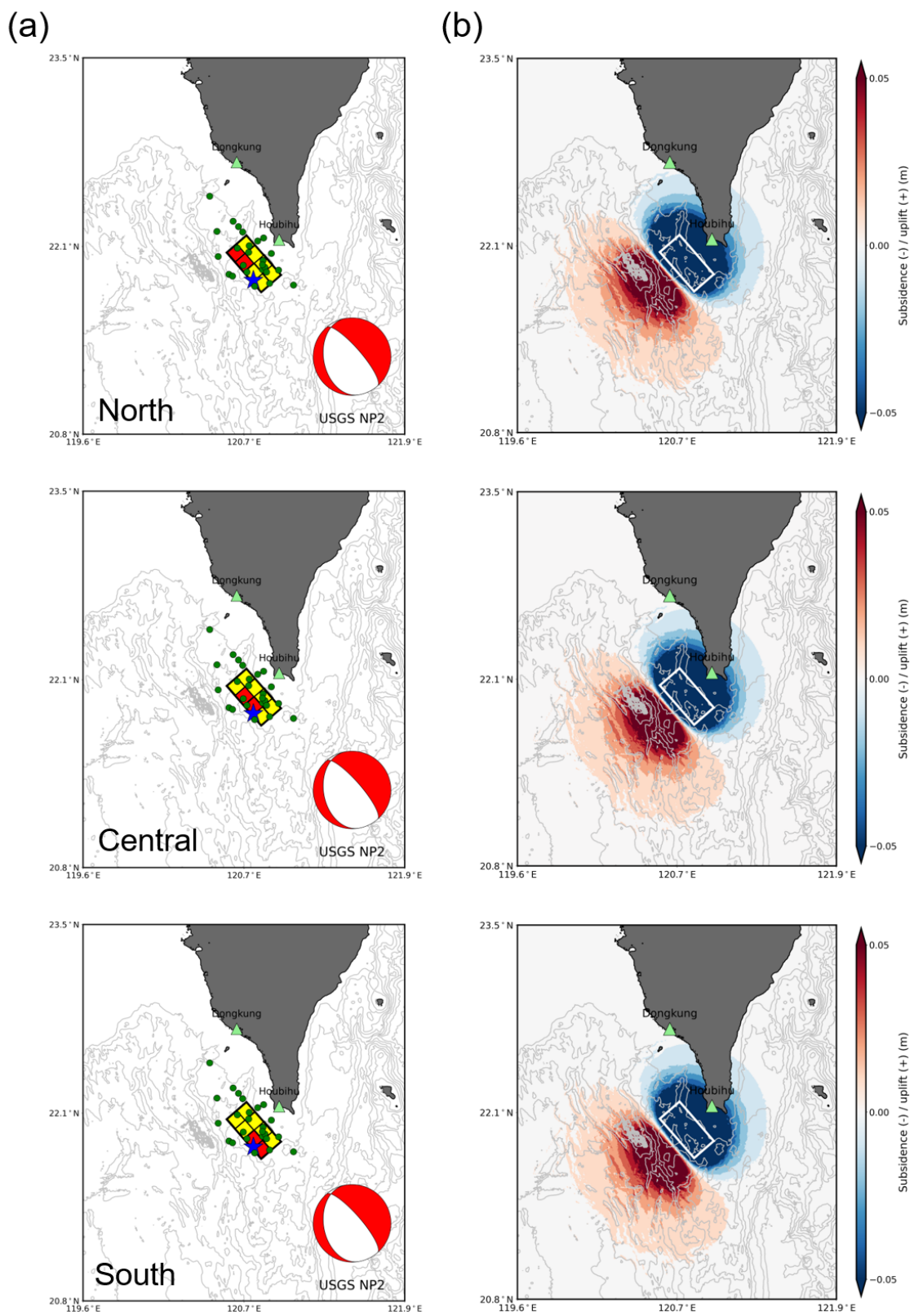
873

874 **Table 4b. Asperity locations of multiple fault models for the two earthquakes.**

Scenario	Asperity location of Earthquake 1			Asperity location of Earthquake 2		
	North	Central	South	North	Central	South
LS1	○				○	
LS2		○			○	
LS3			○		○	
LS4	○			○		
LS5		○		○		
LS6			○	○		
LS7	○					○
LS8		○				○
LS9			○			○

875

876



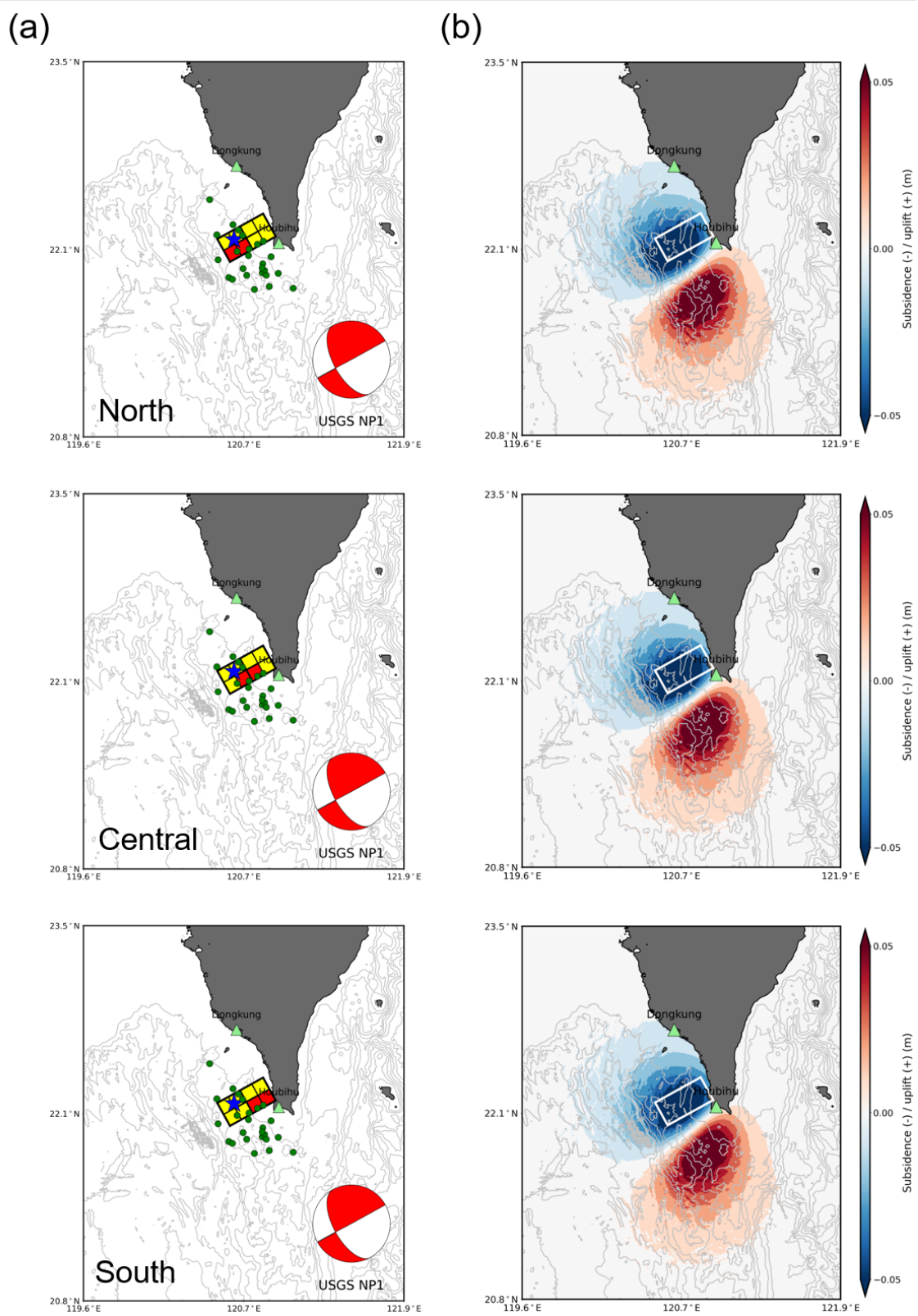
877

878

879

Figure 5. (a) Map of subfault boundaries with different asperity locations for the first earthquake (M_w 7.0). (b) Coseismic crustal vertical displacement calculated using the fault

880 **parameters of the subfaults. The beachball denotes the focal mechanisms of USGS's NP2 nodal**
881 **planes for the first earthquake. The subfaults in red represent large slip areas, and the subfaults**
882 **in yellow represent background slip areas. The large slip area was located only at the shallow**
883 **part of the entire fault area. The blue stars represent the epicenter of the first earthquake, and**
884 **the green circles represent the aftershocks. The tide gauge stations are plotted as green triangles.**
885



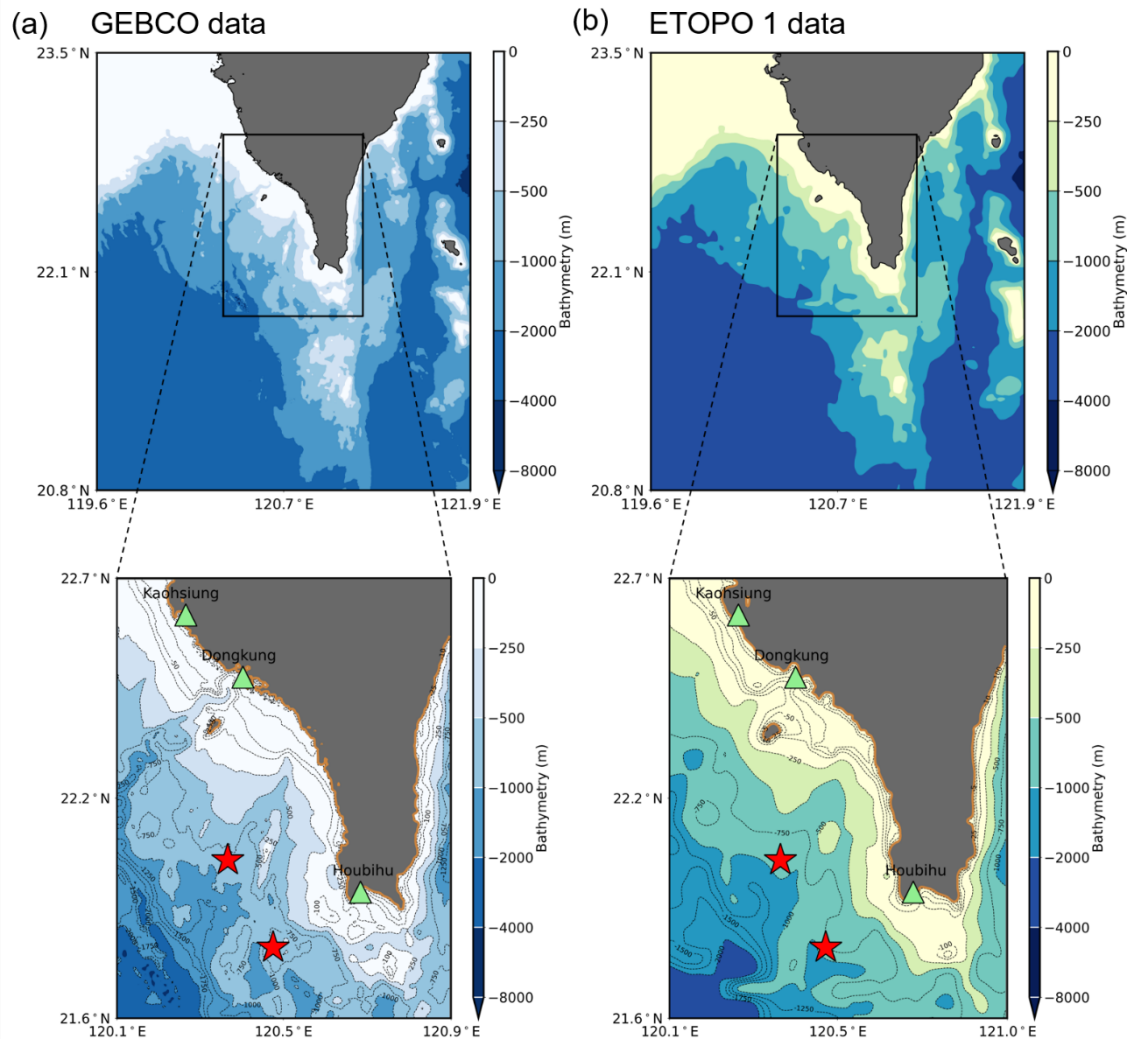
886

887

888

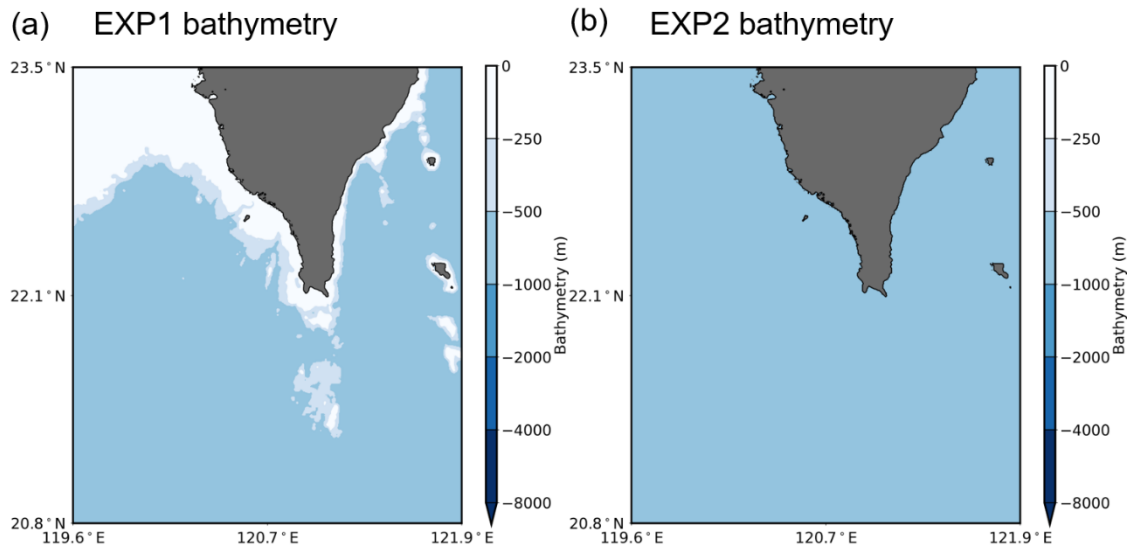
Figure 6. (a) Map of subfault boundaries with three different locations of large slip areas for the second earthquake (M_w 6.9). (b) Coseismic crustal vertical displacement calculated using the

889 **fault parameters of the subfaults. The beachball denotes the focal mechanisms of USGS's NP2**
890 **nodal planes for the first earthquake. The subfaults in red represent large slip areas, and the**
891 **subfaults in yellow represent background slip areas. The large slip area was located only at the**
892 **shallow part of the entire fault area. The blue stars represent the epicenter of the first earthquake,**
893 **and the green circles represent the aftershocks. The tide gauge stations are plotted as green**
894 **triangles.**
895



896
 897
 898
 899
 900

Figure 7. Bathymetry map of the model domain from GEBCO and ETOPO1 bathymetry data. The green triangles denote the locations of the tide gauge stations. The red stars represent the epicenters of the two earthquakes.



901

902

903

904

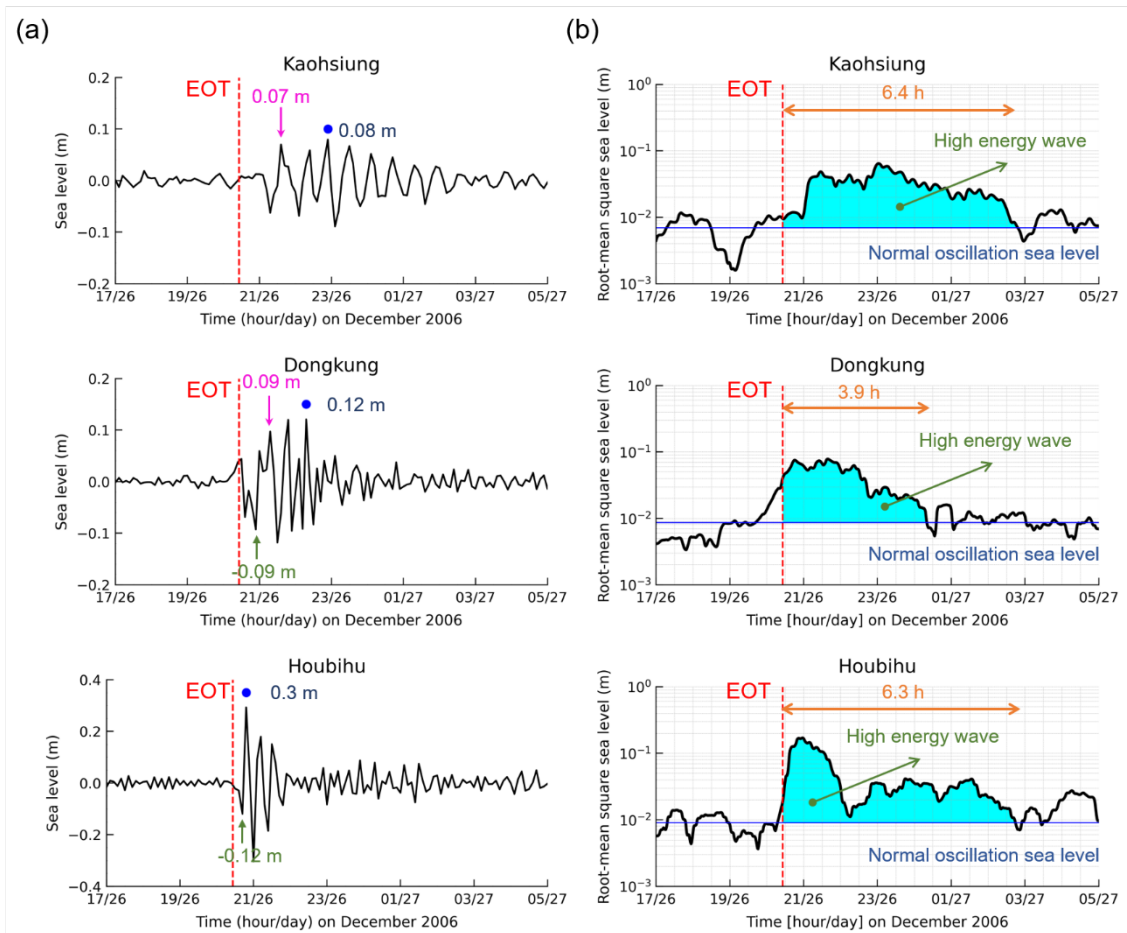
Figure 8. Maps of the manipulated bathymetry of the model domain for numerical experiments (a) EXP1 and (b) EXP2.

905 **Table 5. Details of the bathymetry data used for the numerical experiments MS, EXP1, and**
 906 **EXP2.**

	Numerical experiments		
	MS	EXP1	EXP2
Bathymetry source		GEBCO data	
Grid size		450 m	
Mesh number (x, y)		(538, 631)	
Description of bathymetry conditions	Sea depths from GEBCO data	Sea depths larger than 500 m were replaced with 500 m depths	Sea depths of entire domain were replaced with 500 m depths.

907

908



909

910 **Figure 9. (a) The observed tsunami waveforms and (b) diagrams of root mean square (RMS) sea**
 911 **levels of the 2006 tsunami at the Kaohsiung, Dongkung, and Houbihu tide gauge stations. The**
 912 **vertical, dashed red lines indicate the earthquake occurrence time (EOT). The blue circles**
 913 **denote the arrival of the maximum crest wave that was recorded at all sites. The pink arrows**
 914 **mark the first wave crest. The green arrows represent the trough sign of the first wave arrival.**
 915 **The blue solid lines represent the normal oscillation sea level before the tsunami arrived (i.e.,**
 916 **the mean value of sea level before the earthquake occurrence). The high-energy wave is**
 917 **illustrated in cyan blue-shaded areas. The orange arrows show the elapsed time of tsunami**
 918 **duration.**

919

920 **Table 6a. Details of the tide gauge stations and physical characteristics of tsunami waveforms**
 921 **during the 2006 tsunami.**

Station	Longitude (° E)	Latitude (° N)	Tsunami wave amplitude (m)		
			First trough sign	First wave crest	Maximum wave crest
Kaohsiung	120.28	22.61	-0.06	0.07	0.08
Dongkung	120.43	22.46	-0.09	0.09	0.12
Houbihu	120.74	21.94	-0.12	0.3	0.3

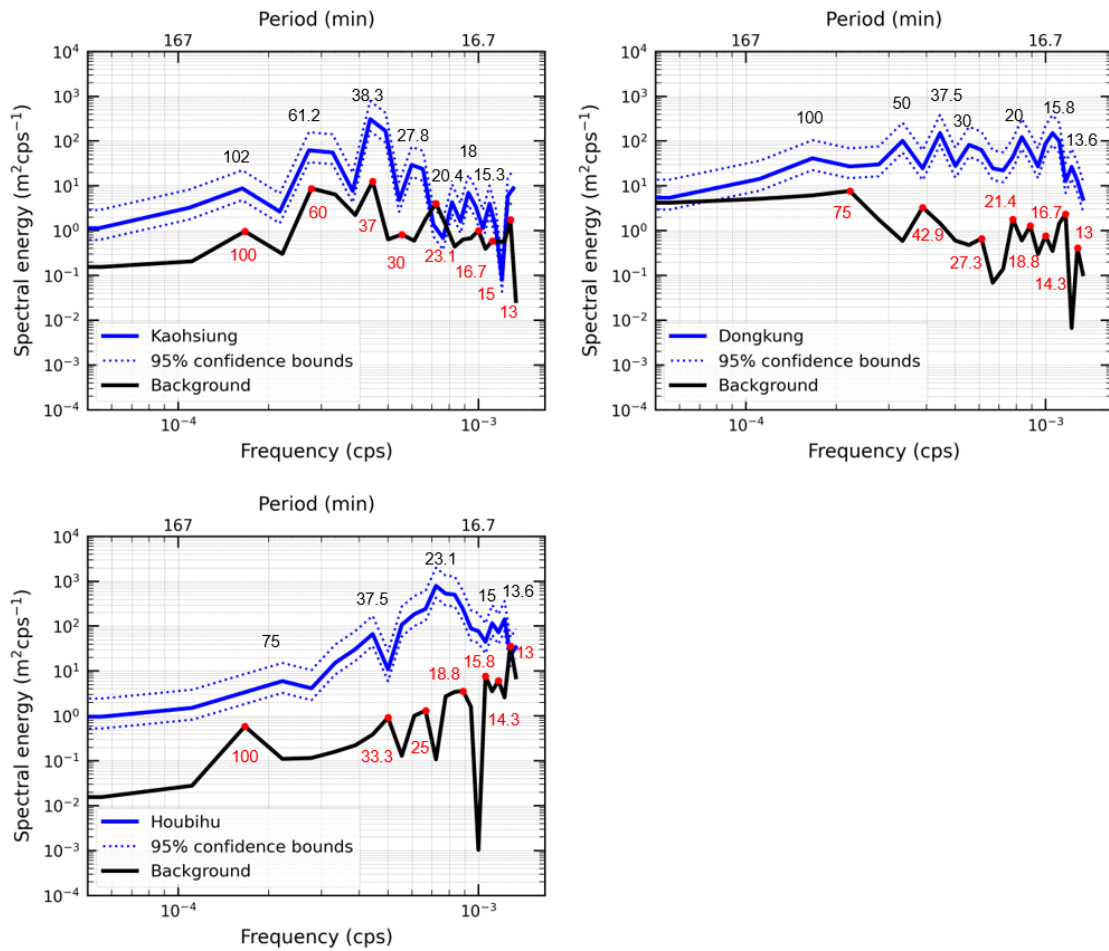
922

923 **Table 6b. Details of the tide gauge stations and physical characteristics of tsunami waveforms**
 924 **during the 2006 tsunami.**

Station	Arrival time (Taiwan Standard Time)			Delay of maximum wave crest (min)	Visible wave period (min)
	First trough sign	First wave crest	Maximum wave crest		
Kaohsiung	21:18	21:44	22:54	70	30-48
Dongkung	20:54	21:18	22:18	60	18-24
Houbihu	20:42	20:48	20:48	0	18-24

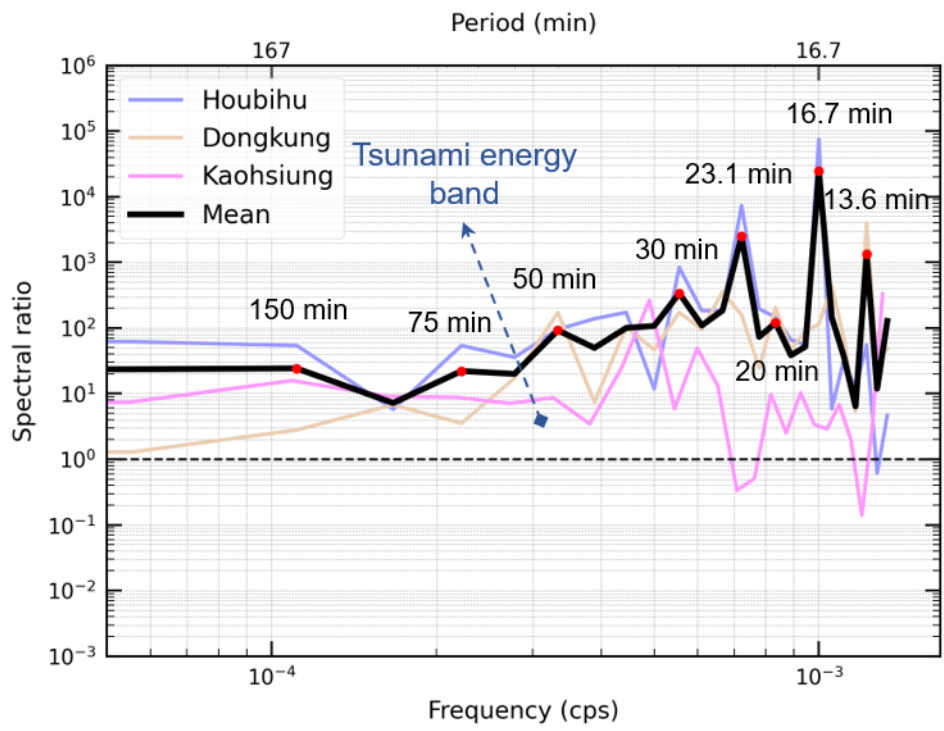
925

926



927

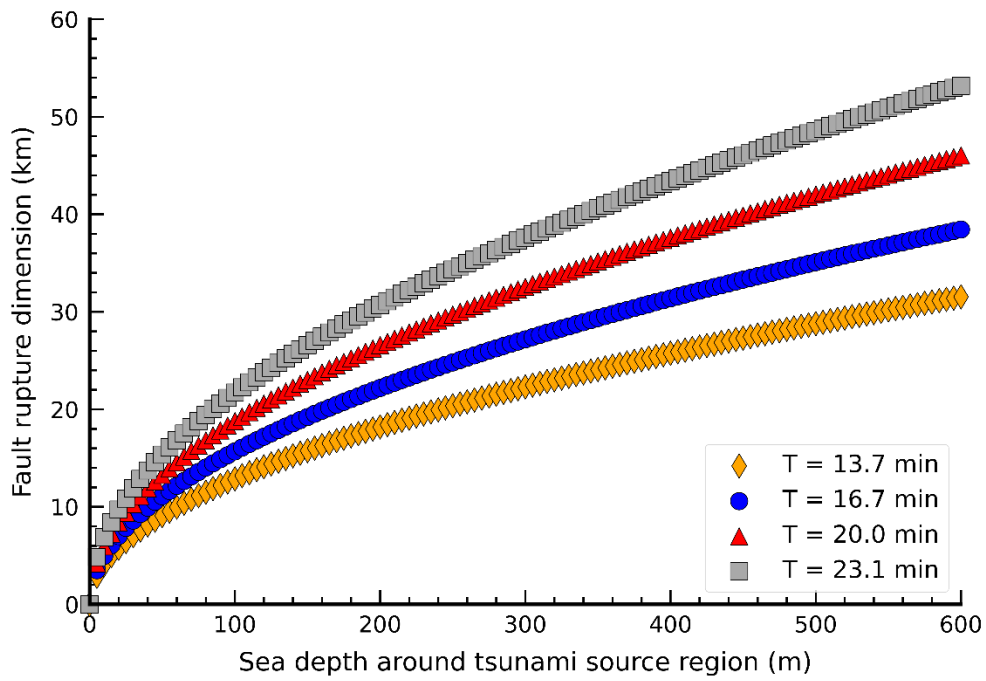
928 **Figure 10. Respective spectra of the observed tsunami waveform (solid blue lines) at each tide**
 929 **gauge station. The solid black lines are spectra for the background signals before tsunami**
 930 **arrivals at each station. The red circles denote the dominant periods of the background spectra.**
 931



932

933 **Figure 11. Respective spectral ratio for the tide gauge spectra. The solid black line is the**
 934 **calculated mean spectral ratio of the three tide gauge spectra. The red circles represent the**
 935 **dominant periods of the mean spectral ratio.**

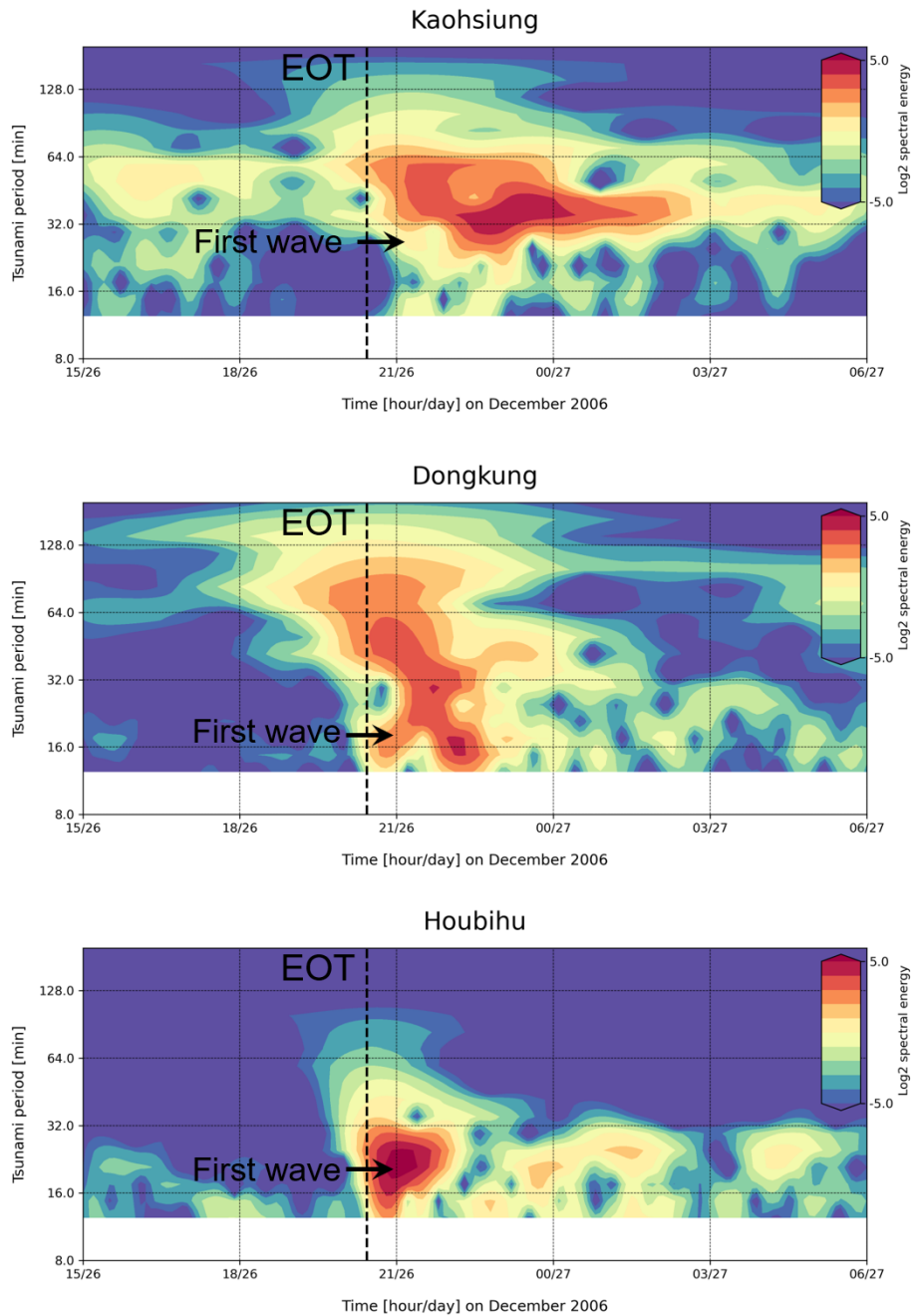
936



937

938 **Figure 12. Correlation of earthquake fault dimensions and sea depth around the tsunami**
 939 **source region derived from the empirical formula proposed by Rabinovich (1997).**

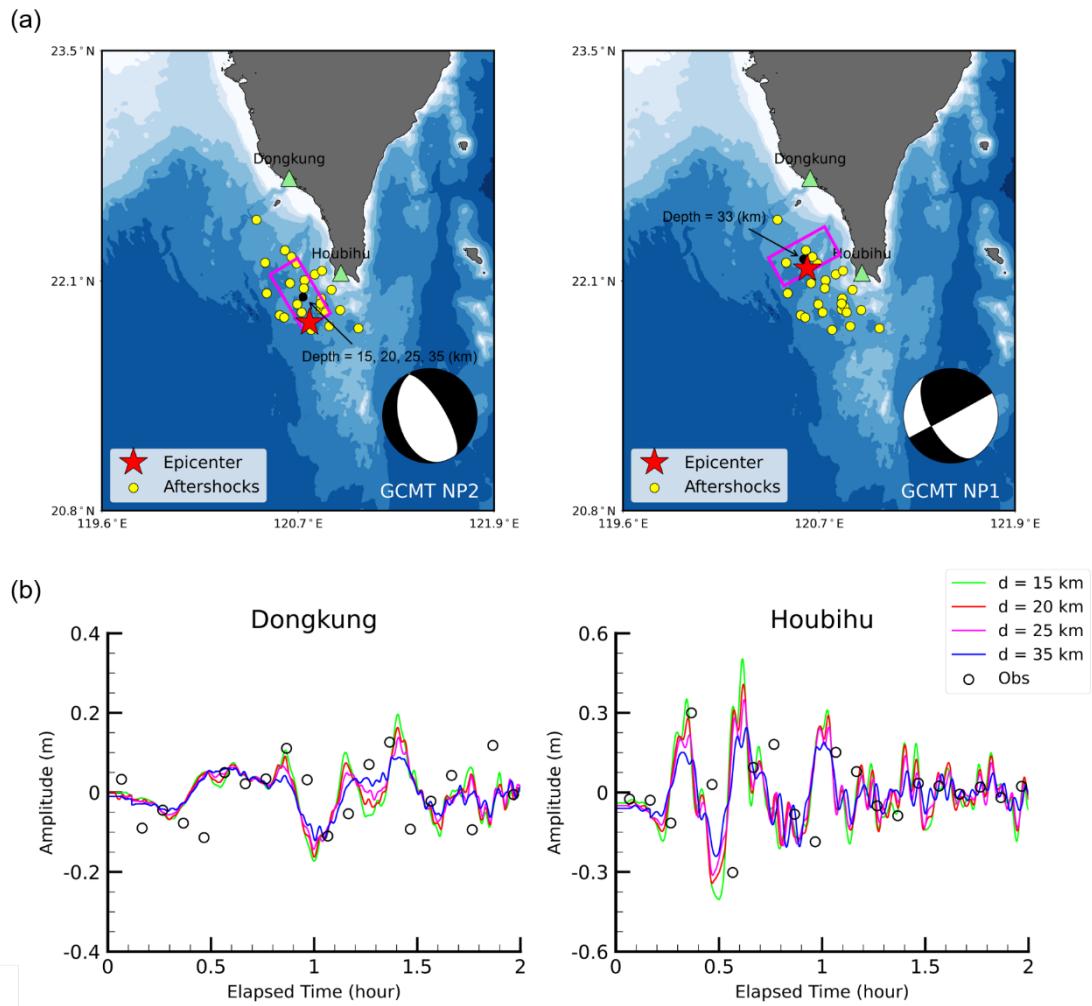
940



941

942 **Figure 13. Wavelet (time-frequency) diagrams of tsunami data for the 26 December 2006**
 943 **tsunami event at the (a) Kaohsiung, (b) Dongkung, and (c) Houbihu tide gauge stations. The**
 944 **colormap represents the log₂ spectral energy at various times and tsunami periods. The vertical,**
 945 **dashed black lines indicate the earthquake occurrence time (EOT). The black arrows denote the**
 946 **arrival time of the first tsunami wave at each station.**

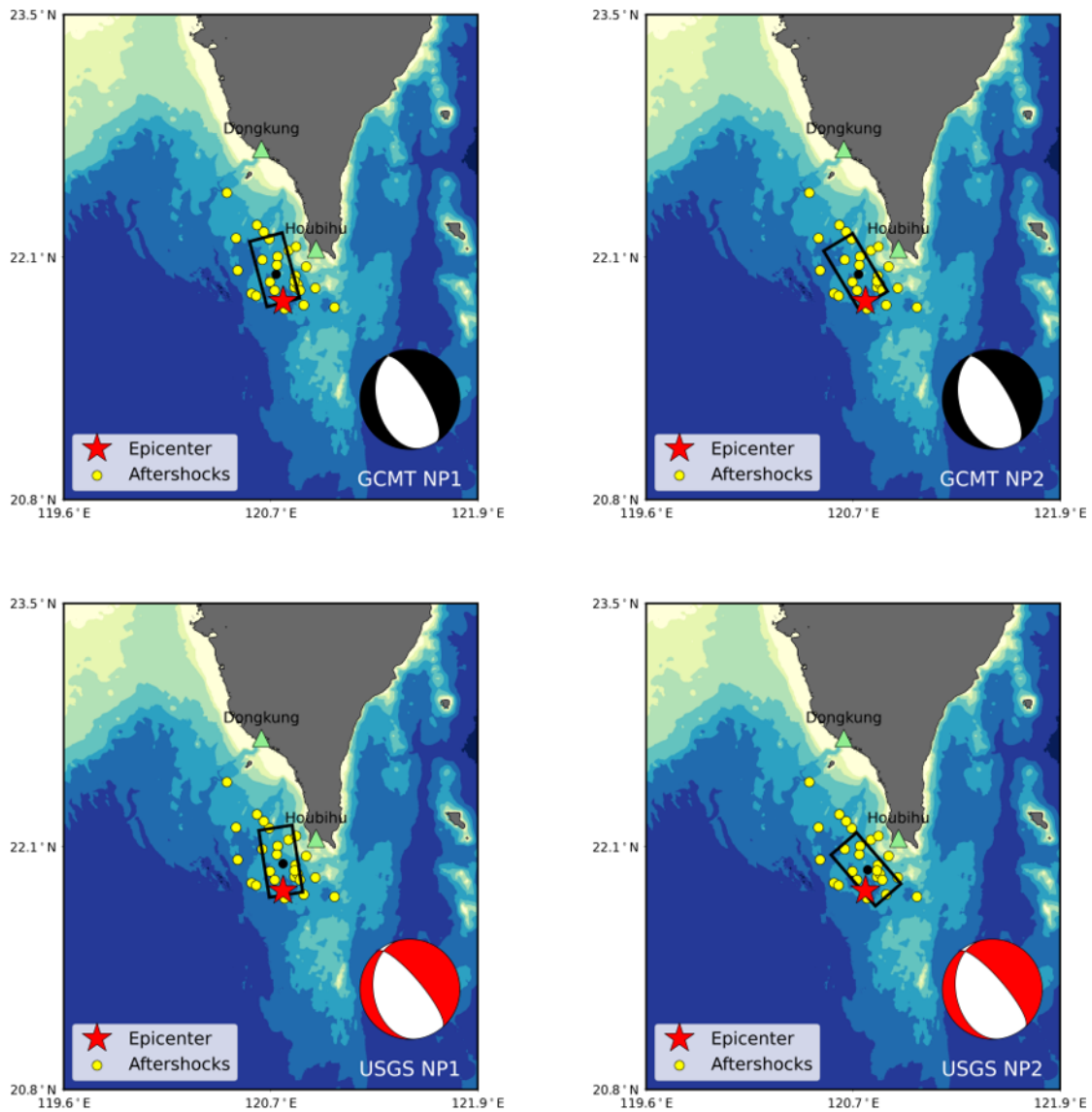
947



948

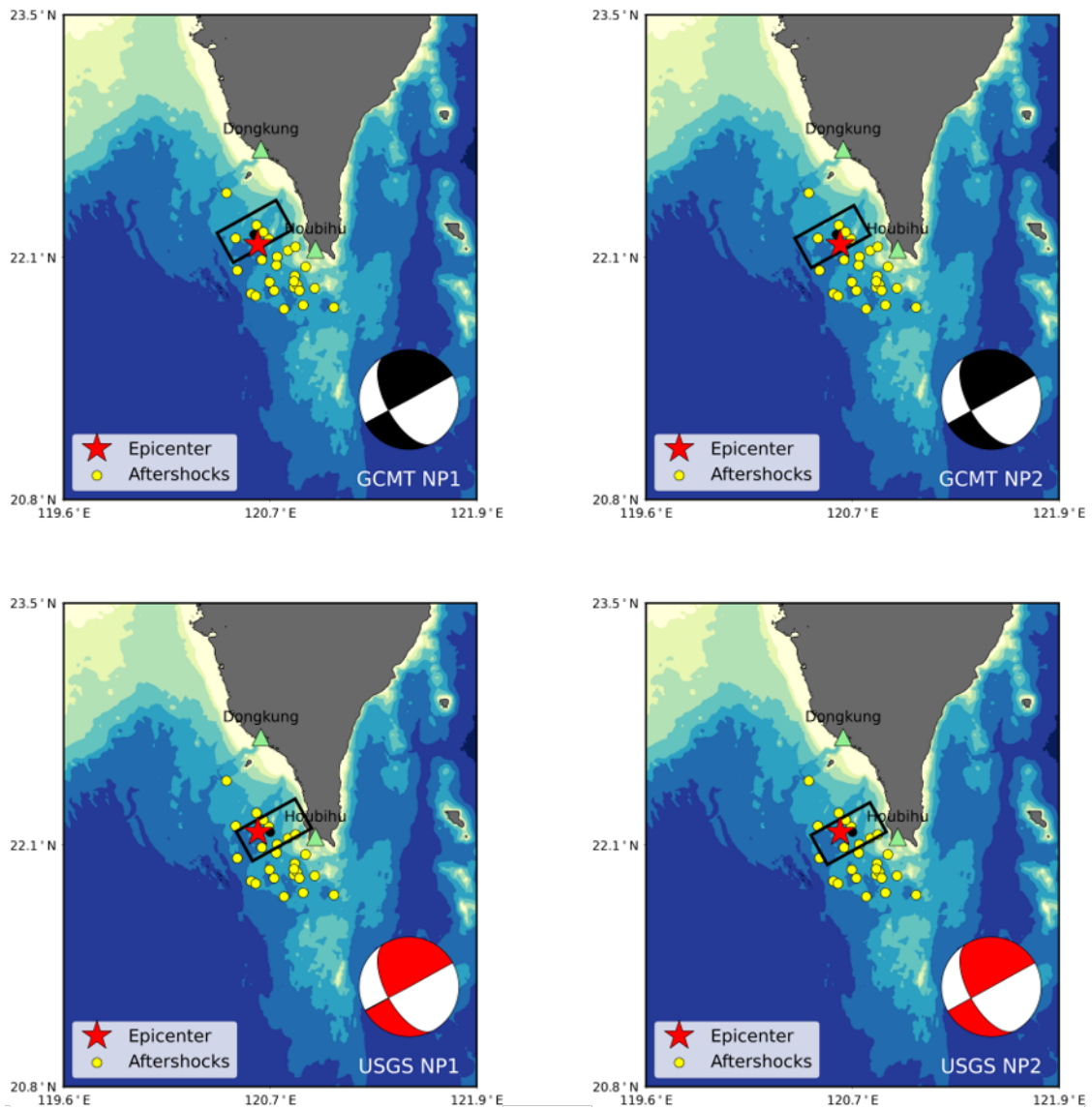
949 **Figure 14. (a) Single fault models with fault dimensions (length \times width) of 40 km \times 20 km of the**
 950 **first earthquake using the GCMT NP2 nodal plane and the second earthquake using the GCMT**
 951 **NP1 nodal plane. The central fault depths of the single fault models for the first earthquake are**
 952 **set as 15 km, 20 km, 25 km, and 35 km, and the central fault depth is fixed at 33 km for the single**
 953 **fault models of the second earthquake for the tsunami sensitivity test. (b) Observed and**
 954 **simulated tsunami waveforms at the Dongkung and Houbihu stations using single fault models**
 955 **with the different central fault depths of the first earthquake.**

956



957
 958
 959
 960
 961

Figure 15. Simple fault models of the first earthquake (M_w 7.0) using the focal mechanisms from GCMT and USGS. The green triangles indicate the tide gauge stations, red stars indicate the epicenter, yellow circles indicate aftershocks, and the black rectangles indicate the fault model.



962
 963
 964
 965
 966
 967
 968

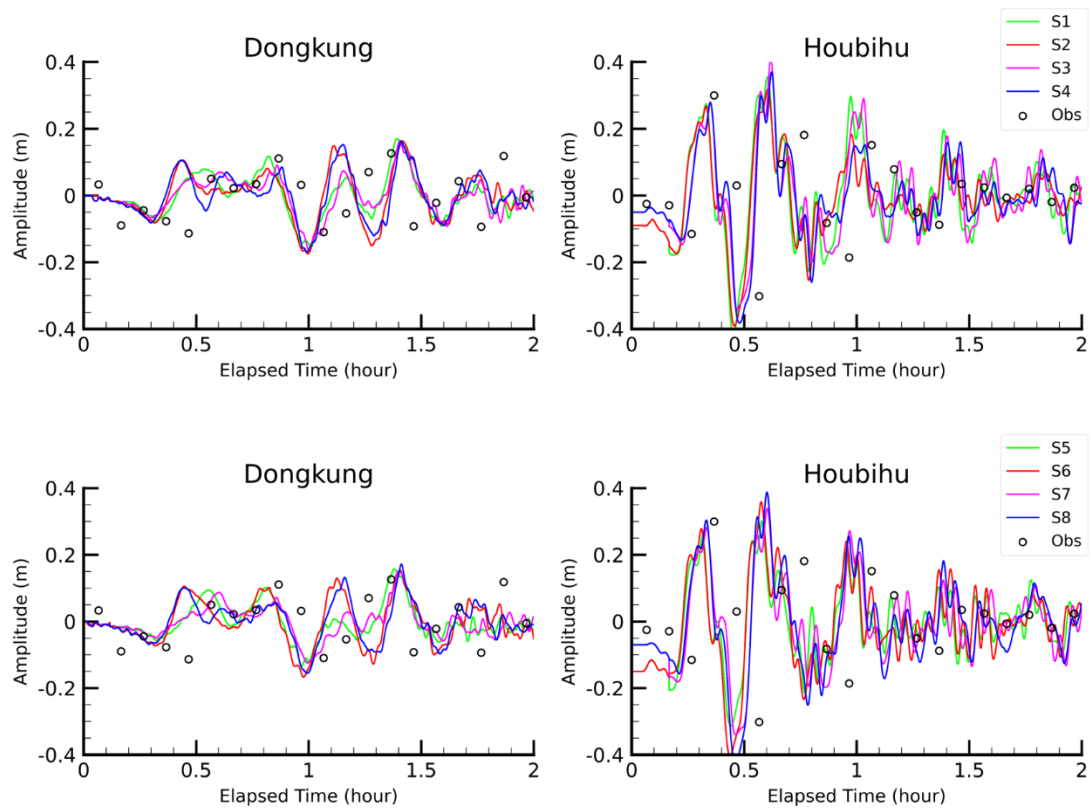
Figure 16. Simple fault models of the second earthquake (M_w 6.9) using the focal mechanisms from GCMT and USGS. The green triangles indicate the tide gauge stations, red stars indicate the epicenter, yellow circles indicate aftershocks, and the black rectangles indicate the fault model.

969 **Table 7. Validation of the simulated tsunami waveforms using single fault models with eight**
 970 **different models of focal mechanisms estimated by GCMT and USGS.**

Scenario	Moment tensor solution	Nodal plane		Misfit of simulated tsunami waveforms
		Earthquake 1	Earthquake 2	
S1	GCMT	NP1	NP1	0.591
S2		NP1	NP2	0.632
S3		NP2	NP1	0.530
S4		NP2	NP2	0.661
S5	USGS	NP1	NP1	0.529
S6		NP1	NP2	0.604
S7		NP2	NP1	0.493
S8		NP2	NP2	0.735

971

972



973

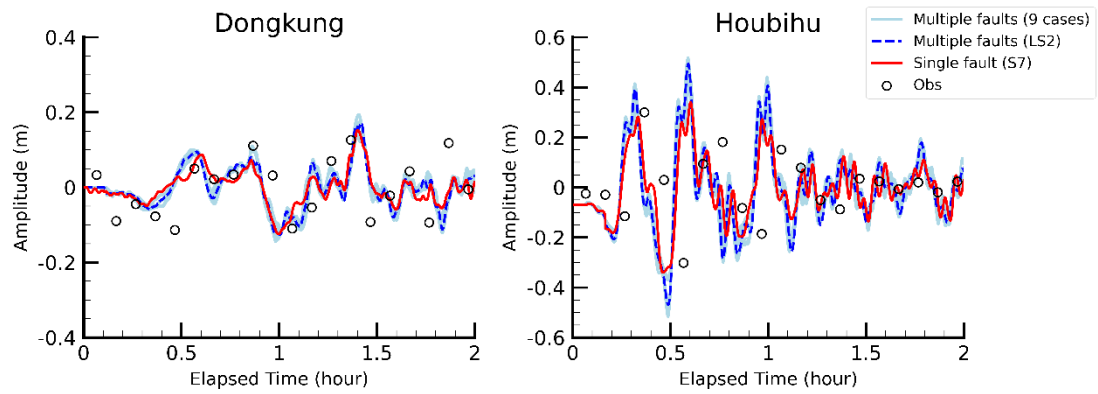
974

975

976

977

Figure 17. Comparison of simulated tsunami waveforms at the Dongkung and Houbihu stations using single fault models with eight different models of focal mechanisms estimated by GCMT and USGS.



978

979

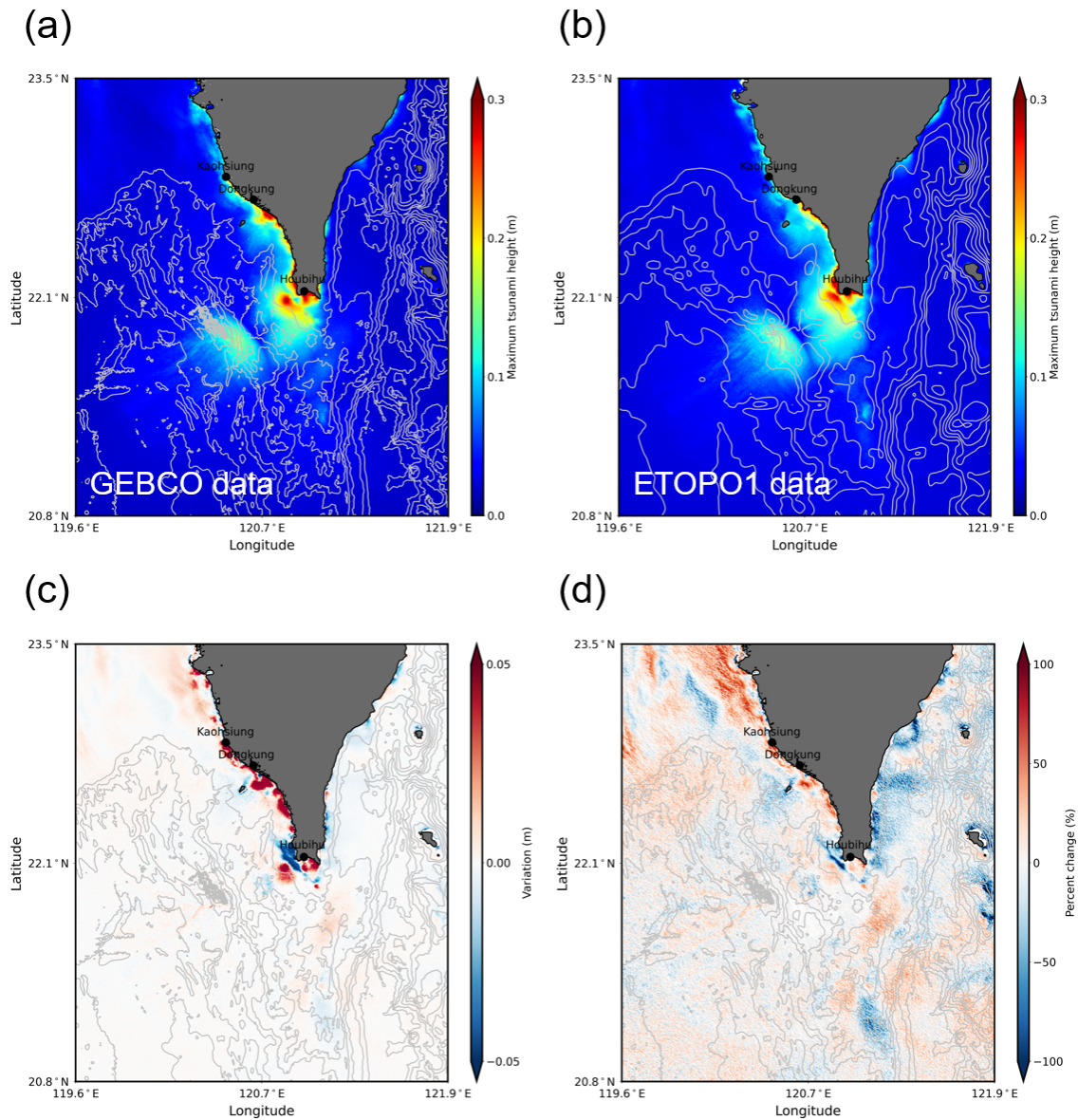
980

981

982

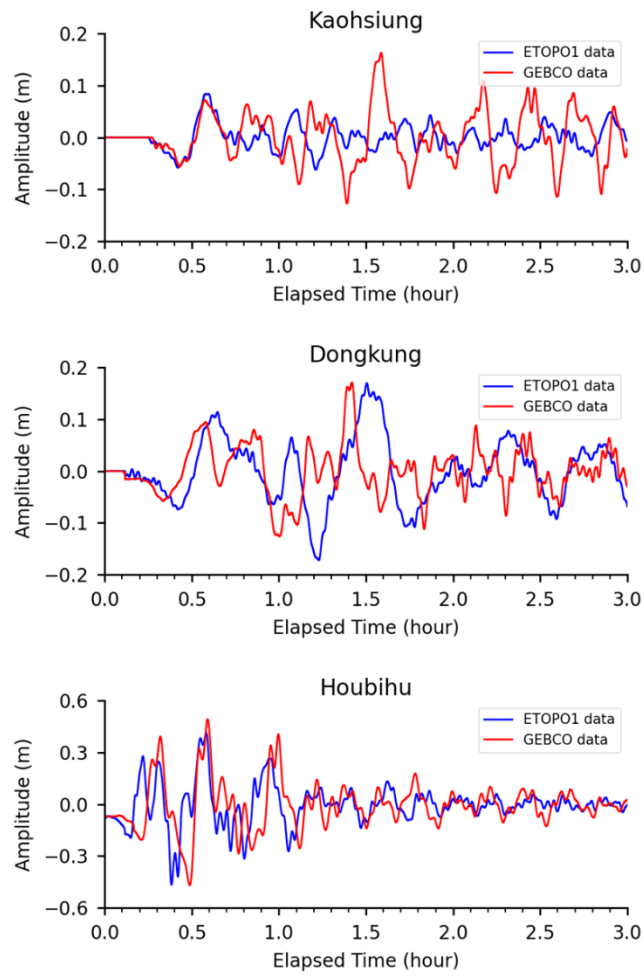
983

Figure 18. Comparison of simulated tsunami waveforms at the Dongkung and Houbihu stations using 9 cases of multiple fault models (solid blue lines) and a single fault model of S7 (solid red lines). The simulated tsunami waveforms using the multiple fault model (LS2) are shown as dashed blue lines. The white circles represent the observational data.



984
 985
 986
 987
 988
 989
 990

Figure 19. Simulated maximum tsunami height using open-source bathymetry data: (a) GEBCO and (b) ETOPO1 data. (c) The variation and (d) the percent variation in the simulated maximum tsunami height using two sources of bathymetry data. The black circles indicate the locations of the tide gauge stations. The bathymetry contour is 500 m based on the GEBCO or ETOPO1 bathymetric data.



991

992 **Figure 20. Simulated tsunami waveforms at the (a) Kaohsiung, (b) Dongkung, and (c) Houbihu**
 993 **stations using two different open-source bathymetry datasets, GEBCO and ETOPO1.**

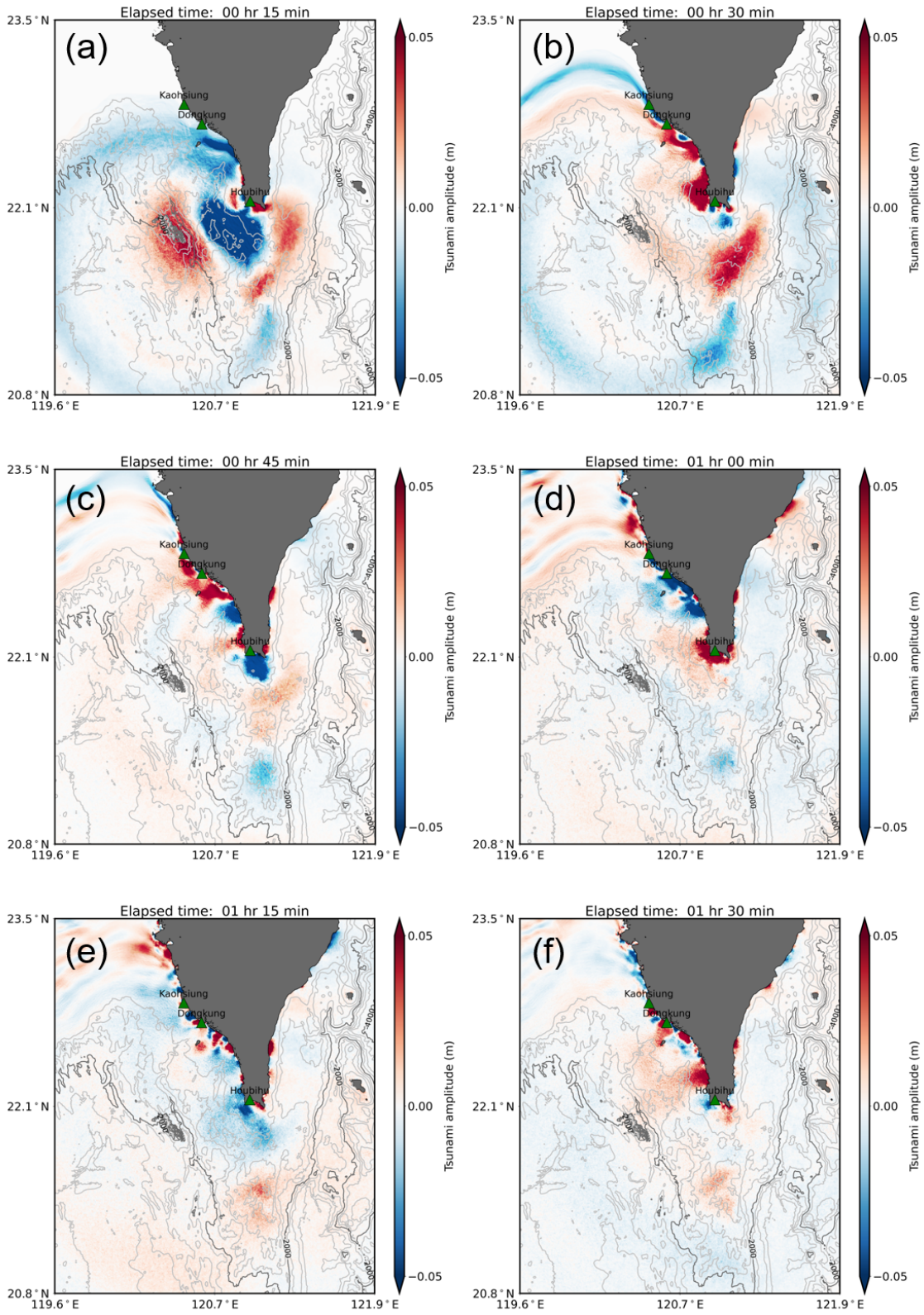
994

995 **Table 8. Details of the locations of the simulated tsunami waveforms and misfit of model**
 996 **results using different open-source bathymetry data at three tide gauge stations.**

Station	Sea depth (m)		Simulated wave peak (m)		Var_{peak}	$\%Var_{peak}$
	GEBCO	ETOPO1	GEBCO	ETOPO1		
Kaohsiung	10	8	0.163	0.084	0.079	48.45
Dongkung	9	14	0.171	0.17	0.001	0.58
Houbihu	4	11	0.493	0.414	0.079	16.02

997

998

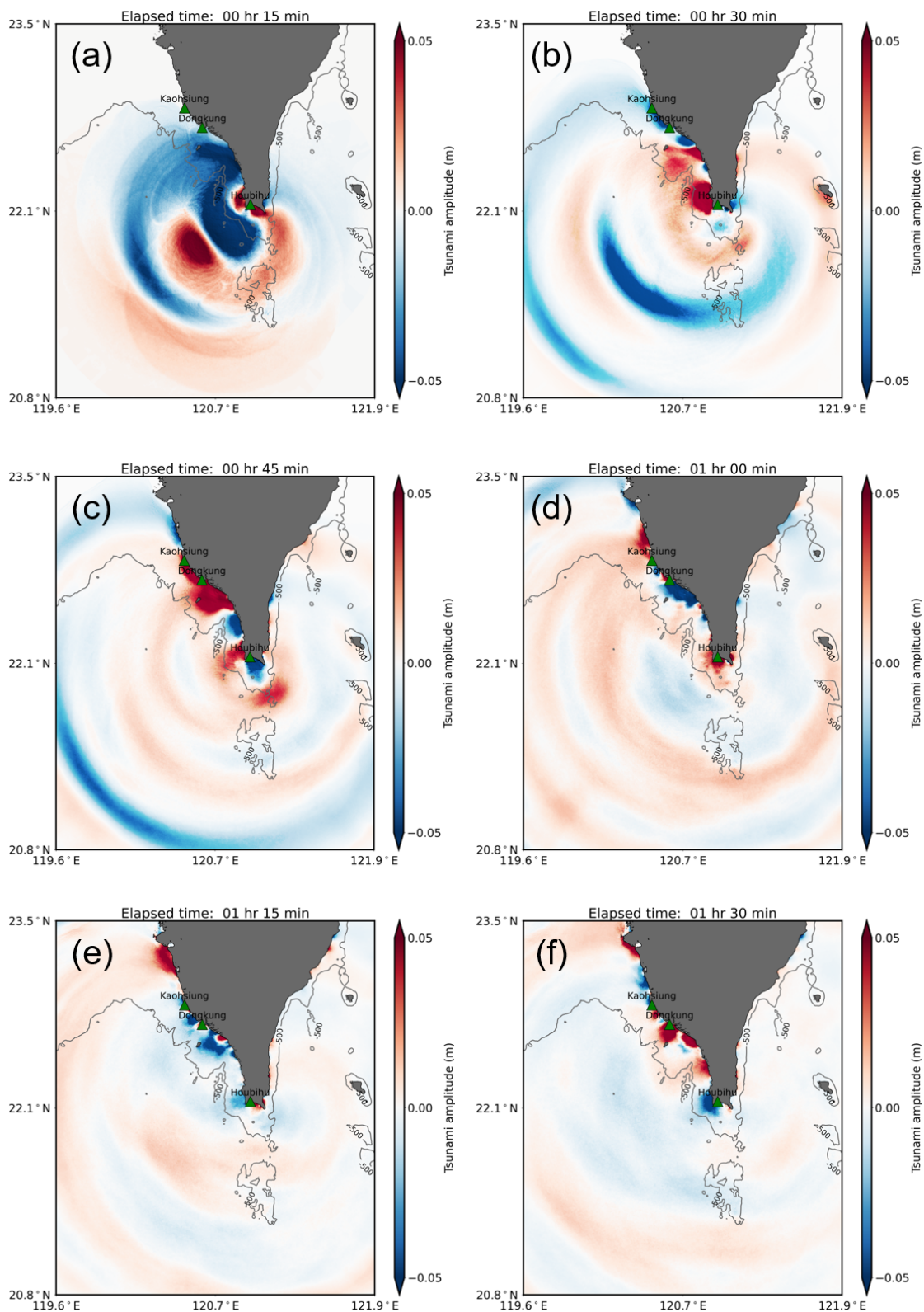


999

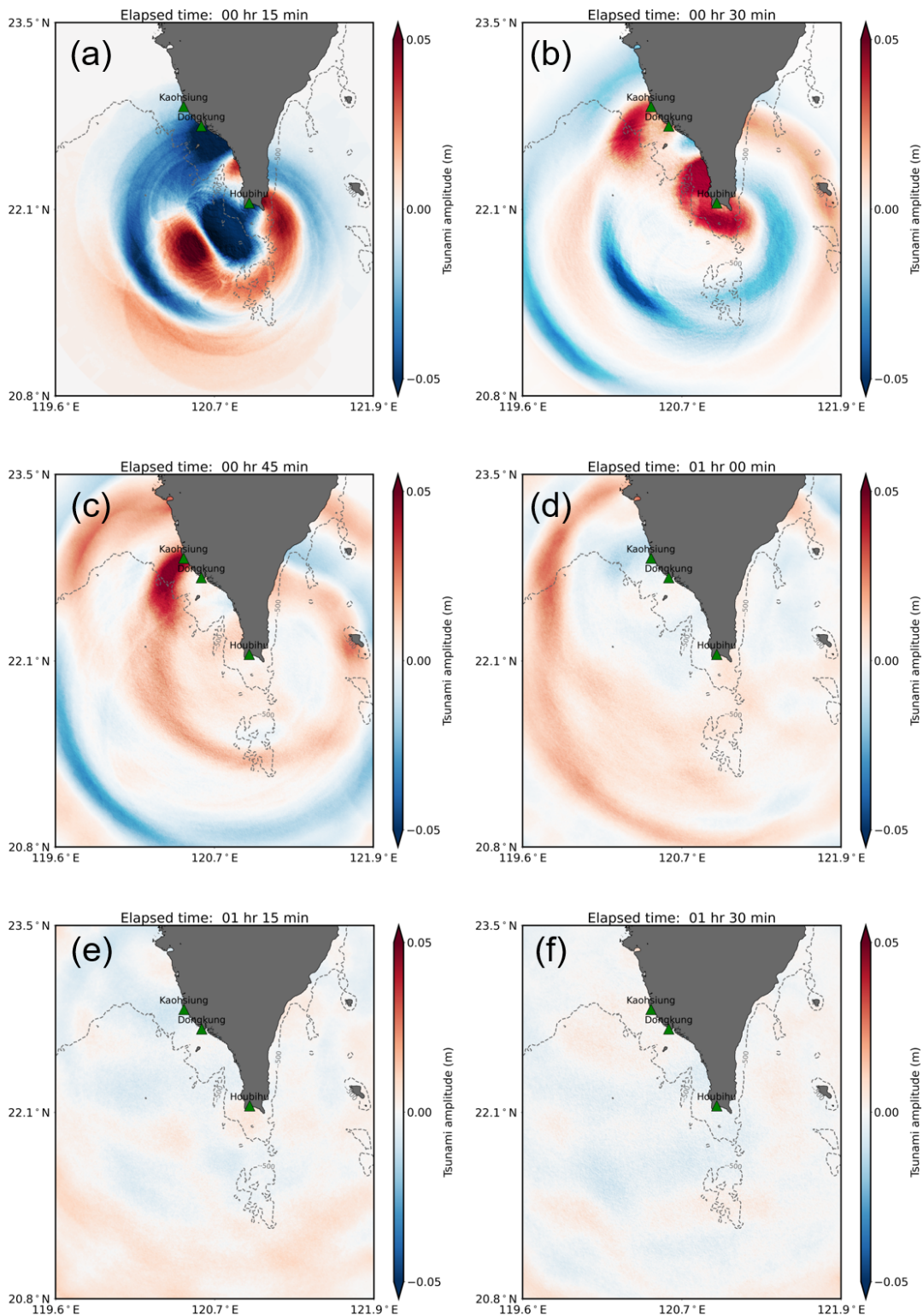
1000

1001

Figure 21. Tsunami propagation snapshots from the numerical experiment MS. The tide gauge stations are plotted in green triangles. The bathymetry contour is 500 m.

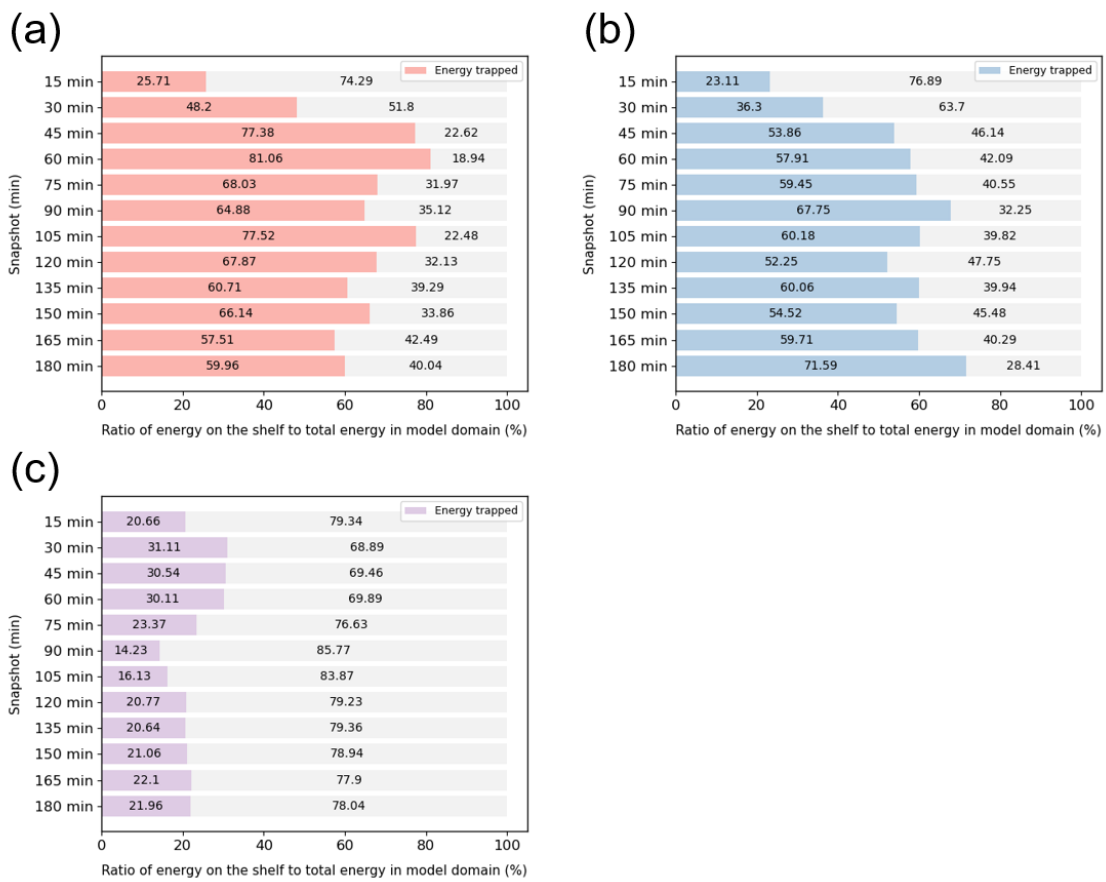


1002
 1003 **Figure 22. Tsunami propagation snapshots from the numerical experiment EXP1. The tide gauge**
 1004 **stations are plotted as green triangles. The bathymetry contour at a depth of 500 m is shown as**
 1005 **a solid gray line.**



1006
 1007
 1008
 1009
 1010

Figure 23. Tsunami propagation snapshots from the numerical experiment EXP2. The tide gauge stations are plotted as green triangles. The corresponding bathymetry contour of 500 m depth from GEBGO data is shown as a dashed gray line.

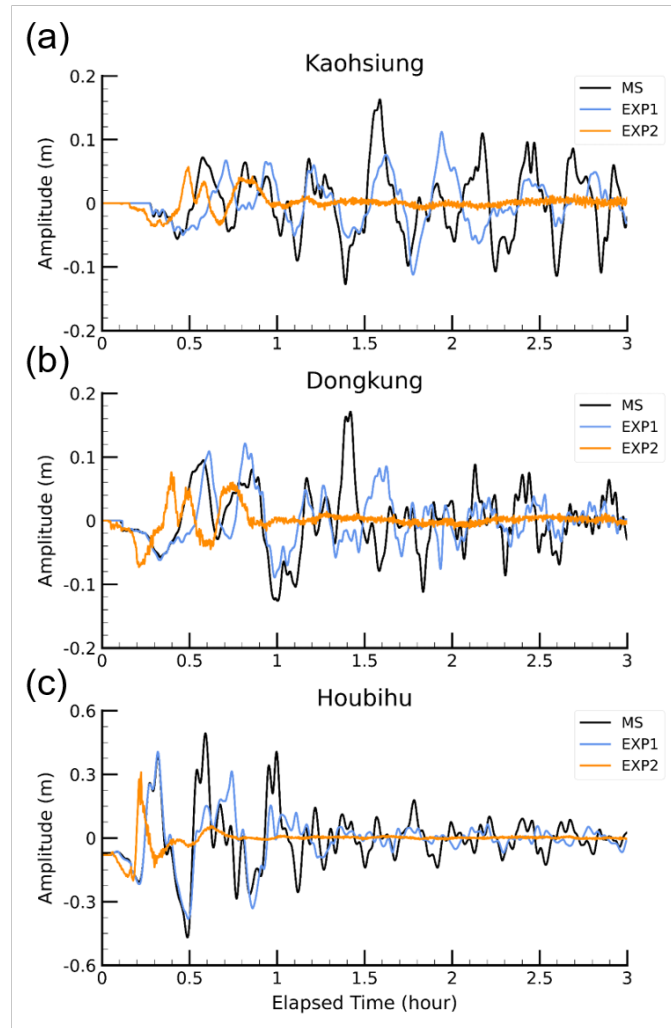


1011

1012 **Figure 24. Trapped ratio of tsunami wave energy calculated from tsunami propagation**

1013 **snapshots every 15 min from numerical experiments (a) MS, (b) EXP1, and (c) EXP2.**

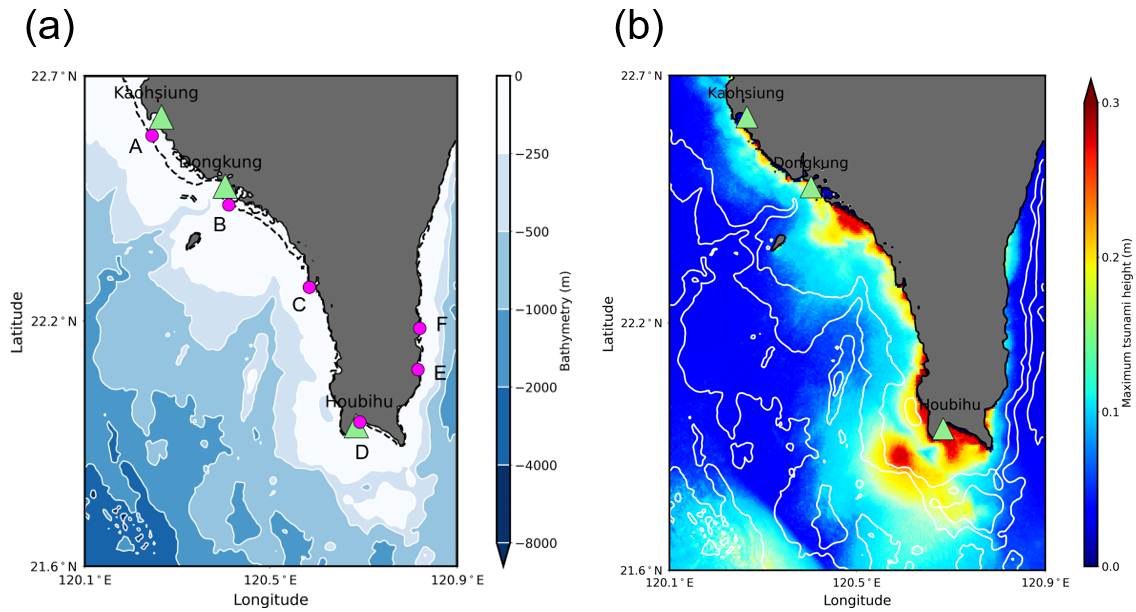
1014



1015

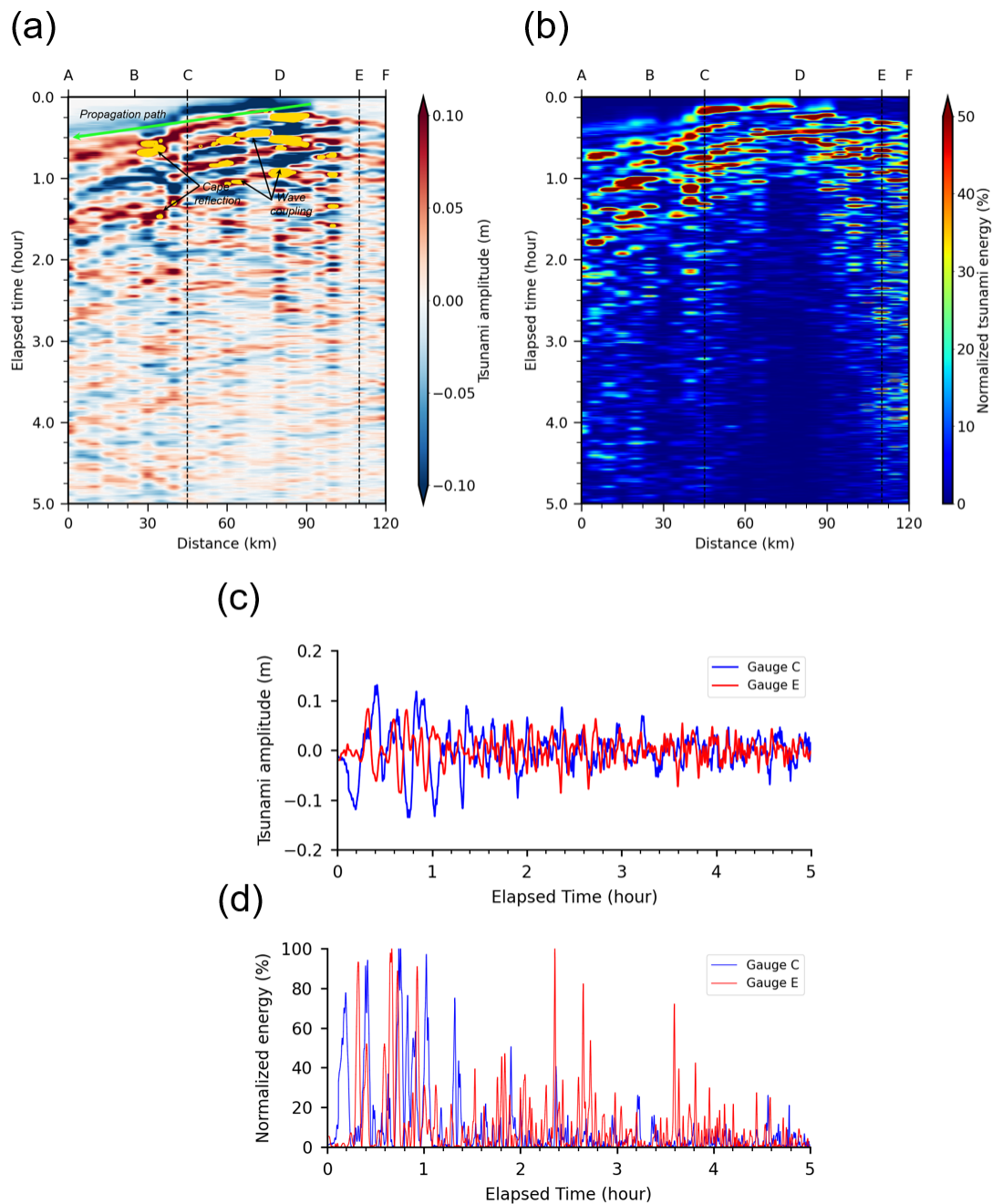
1016 **Figure 25. Simulated tsunami waveforms at the (a) Kaohsiung, (b) Dongkung, and (c) Houbihu**
 1017 **stations from numerical experiments MS, EXP1, and EXP2.**

1018



1019
 1020
 1021
 1022
 1023
 1024
 1025

Figure 26. Zoomed map of the (a) bathymetry around southern Taiwan and (b) simulated maximum tsunami height using a multiple fault model (LS2). Green triangles indicate the locations of tide gauge stations, and pink circles denote numerical wave gauges at a sea depth of 20 m. The solid white lines are contour lines, and the dashed black line represents the bathymetric contour at a depth of 20 m.



1026

1027 **Figure 27. Time-distance diagram of the (a) tsunami wave and (b) normalized energy along the**
 1028 **20 m bathymetry contour from numerical wave gauges A to F and time series measurements of**
 1029 **the (c) tsunami amplitude and (d) normalized energy at numerical wave gauges C and E. The**
 1030 **dashed black lines indicate the distances of numerical wave gauges C and E from A. For**
 1031 **interpretation of the references, please refer to Figure 26a.**

1032

1033